PHYSICAL REVIEW D
PARTICLES AND FIELDS

THIRD SERIES, VOLUME 42, NUMBER 5 1 SEPTEMBER 1990

Nucleon neutral-current structure functions

T. S. Mattison,[a] J. Bofill,[b] W. Busza, T. Eldridge,[c] J. I. Friedman, S. Fuess,[b]
M. C. Goodman,[d] H. W. Kendall, T. Lyons, R. Magahiz,[e] A. Mukherjee,[b] L. S. Osborne,
R. Pitt,[f] L. Rosenson, A. Sandacz,[g] M. Tartaglia,[h] F. E. Taylor, R. Verdier,
J. S. Whitaker,[i] and G. P. Yeh[b]
Massachusetts Institute of Technology, Cambridge, Massachusetts 02139

D. Bogert, R. Burnstein,[j] J. G. Morfin, L. Stutte, and J. K. Walker[k]
Fermi National Accelerator Laboratory, Batavia, Illinois 60510

M. Abolins, R. Brock, A. Cohen,[l] J. Ernwein,[m] D. Owen, J. Slate,[c] and H. Weerts
Michigan State University, East Lansing, Michigan 48824
(Received 7 December 1989)

The structure of the nucleon is studied by means of deep-inelastic neutrino-nucleon scattering at high energies through the weak neutral current. The neutrino-nucleon scattering events were observed in a 340-metric-ton fine-grained calorimeter exposed to a narrow-band (dichromatic) neutrino beam at Fermilab. The data sample after analysis cuts consists of 9200 charged-current and 3000 neutral-current neutrino and antineutrino events. The neutral-current valence and sea nucleon structure functions are extracted from the x distribution reconstructed from the measured angle and energy of the recoil-hadron shower and the incident narrow-band neutrino-beam energy. They are compared to those extracted from charged-current events analyzed as neutral-current events. It is shown that the nucleon structure is independent of the type of neutrino interaction, which confirms an important aspect of the standard model. The data are also used to determine the value of $\sin^2\theta_W = 0.238 \pm 0.013 \pm 0.015 \pm 0.010$ for a single-parameter fit, where the first error is from statistical sources, the second from experimental systematic errors, and the third from estimated theoretical errors.

I. INTRODUCTION

The purpose of this experiment was to test the quark-parton model of hadronic structure and the details of the neutral-current neutrino-quark couplings by measuring the weak-neutral-current nucleon structure functions, or equivalently the quark distributions of the nucleon as observed through the weak neutral current.[1] We compared these quark distributions to those observed in deep-inelastic neutrino-nucleon scattering through the charged-current interaction to test the hypothesis that the nucleon quark distributions are the same for both interactions.

In an earlier paper[2] we verified the prediction of the standard SU(2)⊗U(1) model of Glashow-Weinberg-Salam[3] that the ratio of the neutral-current Bjorken-x scaling-variable distribution to that of the charged current, $(d\sigma^{\mathrm{NC}}/dx)/(d\sigma^{\mathrm{CC}}/dx)$, is nearly flat. Several sources of systematic errors canceled in this "ratio test." This paper goes beyond the ratio test by determining the neutral-current quark distribution directly, thereby allowing a more incisive test of the model to be made.

In the current standard SU(3)⊗SU(2)⊗U(1) model of high-energy lepton-hadron processes, deep-inelastic scattering from nucleons is described by quark momentum distributions and couplings of the electroweak effective Lagrangian. The probing leptons in such experiments can be electrons, muons, or neutrinos. The quark distributions themselves cannot be calculated from first principles but are presumably related to the confinement of the quarks inside the nucleon. The QCD theory of strong interactions allows the logarithmic Q^2 dependence of the structure functions at fixed x to be calculated.[4]

The validity of measurements of $\sin^2\theta_W$ in deep-inelastic neutrino-nucleon scattering[5] is grounded on the assumption that the quark distributions in neutral-current and charged-current interactions are the same. Therefore it is important to directly compare the nucleon structure functions of these two interactions. The experimental evidence that quark distributions are universal has been examined in a number of reviews.[6] There are discrepancies on the order of 10% between the integrals of the quark distributions determined with different lepton probes, and in the x dependence of the quark distributions measured in the charged-current and electromagnetic processes. The quark distributions determined in charged-current interactions have been extensively compared with those determined from the deep-inelastic scattering of charged leptons. On the other hand very little data exist on the quark distributions operative in neutral-current neutrino-nucleon scattering.

In charged-current deep-inelastic scattering, the kinematics of an event can be completely determined from the final-lepton energy and angle and the hadronic-shower recoil energy. In neutral-current deep-inelastic scattering, with invisible initial- and final-state neutrinos, the kinematics must be determined solely from the information on the energy and angle of the recoil-hadron shower, as well as knowledge of the incident-neutrino energy from a narrow-band neutrino beam. The diffuse nature of a hadron shower intrinsically limits the shower angle resolution to be much worse than the typical angle resolution for the outgoing muon in charged-current neutrino-nucleon scattering. As a consequence, the extraction of the underlying quark distributions in the neutral-current measurements requires significant unfolding corrections.

The effect of limited resolution in the scaling variable x would be to smear out (hypothetical) fine structure in the true distribution. To recover this fine structure, an unfolding algorithm must amplify the fine structure of the reconstructed distribution. A side effect of this unfolding process is the amplification of the statistical fluctuations in the raw distribution, which become noise superimposed on the unfolded x distribution. Parametric fits can be performed on the unfolded distribution to recover the smooth underlying distribution. An eigenvector analysis of the unfolded distribution can also be used to control the amplification of statistical fluctuations. We have employed both techniques in this analysis.

In this analysis, the neutral-current results are directly compared with the results of charged-current events analyzed as neutral-current events—that is, by ignoring the muon information except to classify events. The comparison of these hadron-shower-based charged-current results with the muon-based analyses of this and other experiments gives an estimate of the systematic errors of the unfolding process.

II. THEORY

The underlying physics of neutrino-nucleon scattering is described by the gauge-boson–quark couplings[7] and the assumed universal internal momentum distribution of the quarks confined inside the nucleon. For neutrino-quark scattering through the charged-current interaction the first-order coupling term is

$$J_\lambda^{\mathrm{CC}} = -i(G_F M_W^2/\sqrt{2})^{1/2}\langle \bar{u}|\gamma_\lambda(1-\gamma_5)|d_\theta\rangle , \qquad (1)$$

where $|u\rangle$ represents the charged $+\frac{2}{3}$ member of a weak isospin doublet, $|d_\theta\rangle$ is a linear combination of charged $-\frac{1}{3}$ quarks of all generations, as prescribed by the Kobayashi-Maskawa[8] matrix, and G_F is the Fermi coupling constant. The charged-current interaction is purely left-handed $(V-A)$. The corresponding neutral-current weak coupling on the other hand is given by

$$J_\lambda^{\mathrm{NC}} = -i/\sqrt{2}(G_F M_Z^2/\sqrt{2})^{1/2} \times \langle \bar{q}|\gamma_\lambda[R_q(1+\gamma_5)+L_q(1-\gamma_5)]|q\rangle , \qquad (2)$$

where the interaction contains both a right-handed $(V+A)$ term $R_q(1+\gamma_5)$ and a left-handed $(V-A)$ term $L_q(1-\gamma_5)$. The strengths of the respective right- and left-handed terms depend on the electroweak factors

$$R_q = -2Q_q \sin^2\theta_W \qquad (3)$$

and

$$L_q = \tau_3 - 2Q_q \sin^2\theta_W , \qquad (4)$$

where τ_3 is the weak isospin of quark q, Q_q is its electric charge, and $\sin^2\theta_W$ is the Weinberg-Salam mixing parameter. The left-handed coupling dominates for the value of $\sin^2\theta_W$ observed in nature. The neutral-current interaction is constructed to preserve quark flavor, representing the experimental fact that there are no observed flavor-changing transitions.

For neutrino-nucleon scattering through either the charged-current or neutral-current interaction, the cross section can be conveniently parametrized by

$$d^2\sigma/dx\,dy = (G_F^2 M E_\nu/\pi)[y^2 x F_1(x,Q^2) + (1-y-Mxy/2E_\nu)F_2(x,Q^2) \pm (y-y^2/2)xF_3(x,Q^2)] , \qquad (5)$$

where $F_1(x,Q^2)$, $F_2(x,Q^2)$, and $xF_3(x,Q^2)$ are nucleon structure functions. In the equation above the + (−) sign refers to neutrino (antineutrino) scattering. The kinematic variables are defined by the following: M is the nucleon rest mass, E_ν is the incident neutrino energy, E_h is the recoil hadronic kinetic energy, $y = E_h/E_\nu$, Q^2 is the square of the four-momentum transferred to the struck quark, and $x = Q^2/2ME_h$. The outgoing lepton would be a muon for charged-current scattering of muon neutrinos, or a muon neutrino for neutral-current scattering.

In the high-energy limit, where heavy-quark thresholds and quark transverse-momentum effects are expected to become small, the structure functions for the charged-current neutrino-nucleon scattering from an isoscalar target can be expressed as[7]

$$F_2^{\mathrm{CC}}(x,Q^2) = x\Sigma(x,Q^2) = xq(x,Q^2) + x\bar{q}(x,Q^2) , \qquad (6)$$

$$xF_3^{\mathrm{CC}}(x,Q^2)=xV(x,Q^2)\pm 2[xc(x,Q^2)-xs(x,Q^2)]\ , \tag{7}$$

$$xV(x,Q^2)=xq(x,Q^2)-x\bar{q}(x,Q^2)\ , \tag{8}$$

where $xq(x,Q^2)$ $[x\bar{q}(x,Q^2)]$ is the total quark [antiquark] distribution function, $xc(x,Q^2)$ and $xs(x,Q^2)$ are the charm- and strange-quark distribution functions, respectively, and $xV(x,Q^2)$ is the valence-quark distribution function. The corresponding neutral-current structure functions are

$$\begin{aligned}F_2^{\mathrm{NC}}(x,Q^2)=&\,(u_L^2+d_L^2+u_R^2+d_R^2)x\Sigma(x,Q^2)\\&-(u_L^2-d_L^2+u_R^2-d_R^2)2[xc(x,Q^2)\\&-xs(x,Q^2)]\ ,\end{aligned} \tag{9}$$

$$xF_3^{\mathrm{NC}}(x,Q^2)=(u_L^2+d_L^2-u_R^2-d_R^2)xV(x,Q^2)\ . \tag{10}$$

The electroweak-coupling terms u_L, d_L are the left-handed Z^0-quark coupling for the charge $\frac{2}{3}$ and $-\frac{1}{3}$ quarks, respectively, and are specific cases of L_q given by Eq. (4) above. The corresponding right-handed couplings u_R and d_R are given by Eq. (3) above.

The structure function $2xF_1(x,Q^2)$ is related to the structure function $F_2(x,Q^2)$ by

$$\begin{aligned}&2xF_1(x,Q^2)\\&\quad=F_2(x,Q^2)(1+4M^2x^2/Q^2)/[1+R_L(x,Q^2)]\ .\end{aligned} \tag{11}$$

The function $R_L(x,Q^2)$ is the ratio of the longitudinal to transverse cross sections. It is difficult to measure, and in precision structure function analyses it is frequently taken to be the calculated QCD function.[9] Within limits of the present experimental accuracy, $R_L(x,Q^2)$ agrees with this theoretical prediction in a Q^2 region where target mass and higher-twist effects are believed to be small.[10] In the limit of high Q^2, it is a reasonable approximation to assume the Callan-Gross relation[11]

$$2xF_1(x,Q^2)=F_2(x,Q^2)\ . \tag{12}$$

The charged-current structure function F_2^{CC} is a pure flavor isosinglet, since at high energies where quark mass effects are small, it depends on all quark flavors in equal weight. The corresponding neutral-current structure function contains a small $xc(x,Q^2)-xs(x,Q^2)$ term. The neutral-current structure function xF_3^{NC} depends only the valence quarks and the weak-neutral-current couplings, whereas the corresponding charged-current structure functions contain the $xc(x,Q^2)-xs(x,Q^2)$ term. But the main difference between the respective neutrino-nucleon scattering modes, aside from overall normalization from the strength of the Z^0-quark coupling, is that of the $V-A$ and $V+A$ structure.

III. APPARATUS AND DATA

The reconstruction of neutral-current events requires knowing the incident neutrino energy, and the energy and angle of the recoil hadronic shower. Therefore the experiment requires a narrow-band neutrino beam, which allows an estimation of the incident neutrino energy, and a detector in which it is possible to distinguish neutral-current and charged-current events and measure the energy and angle of the recoiling hadronic shower. A muon spectrometer enables the outgoing muon momentum to be determined for charged-current events. The reconstructed charged-current events are useful in studying the systematics of the incident narrow-band neutrino beam, the detector, and the calibration and resolution measurements.

A. Narrow-band beam

Data for this experiment were recorded in the Fermilab narrow-band neutrino beam.[12] The layout of the beam line is shown in Fig. 1. The neutrino beam had a distinct dichromatic energy structure in which the higher-energy band was produced by neutrinos from kaon decay, and the lower-energy band, with the more copious neutrino flux, by neutrinos from pion decay. The neutrinos in the narrow-band beam came primarily from the two-body decays $\pi^\pm\to\mu^\pm\nu_\mu$ [branching ratio $(B)\approx 100\%$] and $K^\pm\to\mu^\pm\nu_\mu$ $(B\approx 63.51\%)$. A small background arose from the three-body decay modes of the kaon $(K^\pm\to\pi^0e^\pm\nu_e$, $B\approx 4.82\%$, and $K^\pm\to\pi^0\mu^\pm\nu_\mu$, $B\approx 3.18\%)$ as well as pion and kaon decays before the momentum analysis of the narrow-band beam transport system.

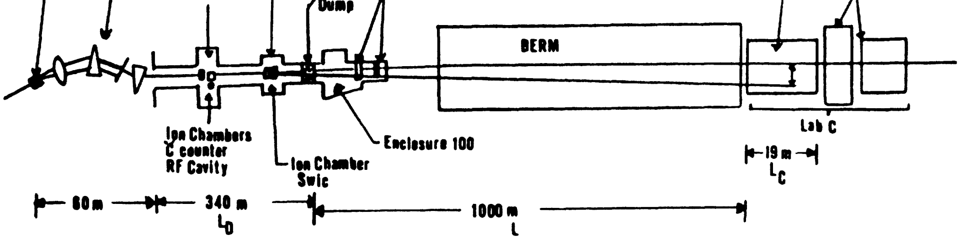

FIG. 1. The layout of the narrow-band beam at Fermilab. Shown is a schematic outline of the beam transport system which defines the momentum of the secondary pions and kaons of the beam, the secondary beam monitors, and the location of the FMM experiment. Note that the drawing is not to scale, although the relevant distances are indicated. For simplicity the other neutrino detectors in the beam are not shown.

For a secondary meson of mass m and laboratory energy E_0 which undergoes decay, the laboratory energy E_ν of the neutrino may be calculated from the laboratory angle θ_ν of the neutrino with respect to the meson-beam direction by

$$E_\nu = 2mE^*/(E_0\theta_\nu^2 + m^2/E_0) , \qquad (13)$$

where E^* is the energy of the neutrino in the meson center-of-mass frame. [For two-body decay of the meson into a neutrino and muon, $E^* = (m^2 - m_\mu^2)/2m$.] Pions and kaons have different E^* and mass, hence their respective decays result in two distinct neutrino energy-radius correlations.

Data were taken at four different secondary momentum settings: antineutrinos (165-GeV/c negative secondaries) and neutrinos (165-, 200-, and 250-GeV/c positive secondaries). Monitor readings from the primary proton and secondary pion and kaon beam line were recorded during data taking. These monitoring devices consisted of ion chambers, an rf cavity, and a secondary-emission monitor to determine the secondary-beam flux. A Cherenkov counter was used to analyze the particle composition at each beam setting thereby determining the π/K ratio which influenced the neutrino flux shape. The monitor data were used to verify that the Monte Carlo simulation of the beam was correct, and were employed in determining the total neutrino-nucleon scattering cross section.[13]

Figure 2 shows the dichromatic energy spectrum of the beam measured from reconstructed charged-current events for the four beam settings of this experiment. The solid histograms are the Monte Carlo–simulated spectra.

The incident neutrino energy of a neutral-current event was inferred by means of the energy-versus-radius correlation of the narrow band beam using the measured radius of the neutrino-nucleon interaction vertex from the central axis of the beam. A detailed Monte Carlo simulation, checked against charged-current data, was used to determine the average neutrino energy from pion and kaon decay at each radius. The neutrinos at small radius in the detector came mostly from pion decay. The larger radius events had a larger component of kaon neutrinos. The energy-versus-radius correlation is illustrated in Fig. 3 which shows $E_\mu + E_h$ from charged-current events plotted versus the radius. Combining all resolution smearing effects from the beam characteristics, the energy resolution for the pion band neutrinos from the energy-versus-radius correlation was about $\sigma E_\nu / E_\nu \approx 15\%$. When the parentage of the incident neutrino was kaon decay but the event was mistakenly analyzed as arising from pion decay, the incident neutrino energy was underestimated by about a factor of 2.

B. The detector

To achieve the fine-grained sampling needed for this experiment we constructed the absorber out of a great many (608) alternating planes of plastic extrusions filled with sand and steel shot interleaved with planes of multicell polypropylene flash chambers with magnetostrictive readout. The flash chambers sampled the shower every

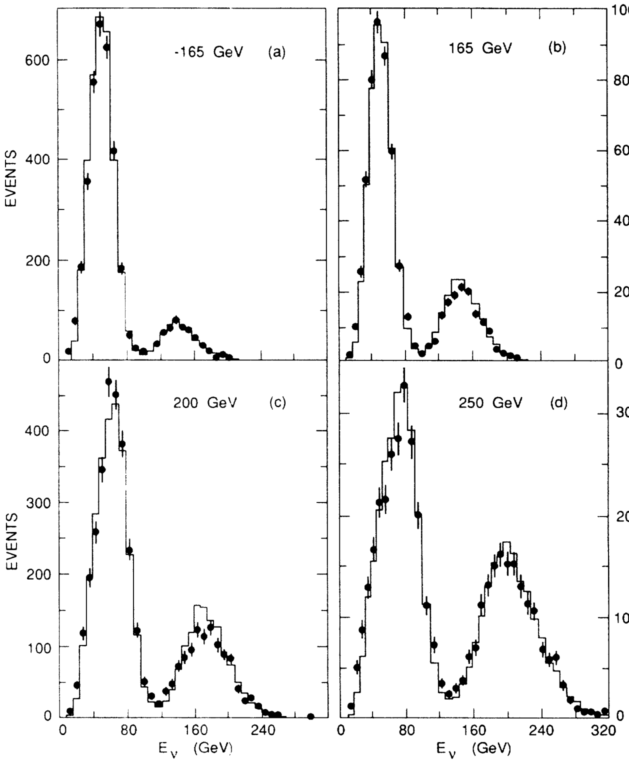

FIG. 2. The dichromatic energy spectrum of the narrow-band beam measured by reconstructed charged-current events. Shown are the spectra at each of the energy settings of the experiment. The Monte Carlo simulations, displayed as smooth lines, have been overlayed for comparison. A small correction to the K/π ratio which was performed in the final analysis is not included in this plot.

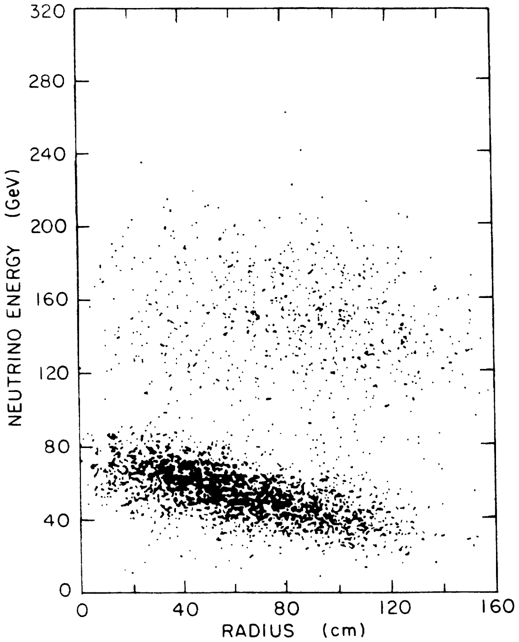

FIG. 3. The energy-versus-radius correlation of the narrow-band beam operated to focus positive secondaries at 165-GeV/c central momentum. The lower band arose from pion decay and the upper from the two-body decay mode of the kaon.

3.7% of an absorption length, and every 22.1% of a radiation length. Flash-chamber cells were at 0° (X chambers) and at 80° and 100° (Y and U chambers) from horizontal, forming an U-X-Y-X pattern.[14]

Proportional tube planes, made from extruded aluminum, were used to trigger the calorimeter and provided an additional determination of the hadronic energy. The planes also generated a trigger signal which was proportional to the number of hit electronic cells in a given plane. One proportional tube plane was placed between each group of 16 flash chamber planes. Alternate planes had horizontal and vertical wires. The wires of the planes were spaced every 2.5 cm, and were tied together electronically in groups of four giving an effective lateral sampling of about one Moliere radius.

A liquid-scintillation counter was placed at the front of the calorimeter to veto muons from upstream neutrino interactions. Other liquid scintillators were located every 80 flash chamber planes to provide a stand-alone cosmic-ray trigger useful for studying the operation of the flash chambers.

The total mass of the calorimeter was about 340 metric tons. The important parameters of the calorimeter are summarized in Table I. Figure 4 shows the general layout of the neutrino detector and the details of one module of the calorimeter.

The muon spectrometer was placed downstream of the calorimeter. It consisted of three 7.3-m- and four 3.7-m-diameter iron toroid magnets. The total length of iron through which a muon could penetrate was about 7 m and the average magnetic-field strength about 13 kG. Among the toroids were four stations of proportional planes. Each station had a staggered double-layer aluminum proportional plane providing a 12.7-mm effective spacing in both horizontal and vertical coordinates. The readout employed a charge division scheme.[15] The momentum resolution of the spectrometer was limited by the multiple scattering of the muons in the iron and was typically $\sigma p_\mu / p_\mu \approx 15\%$.

The trigger for neutral-current data required significant energy deposition in the proportional tube planes in the calorimeter. At least two channels in at least two proportional tube planes were required to be above a threshold to minimize triggers from cosmic-ray muons. The front scintillation counter was used to veto beam-associated muons. The trigger was essentially 100% efficient for showers over 10 GeV. There was an additional trigger with a lower energy threshold in the calorimeter which also required muon hits in the toroid proportional-tube planes. Most charged-current events satisfied both triggers.

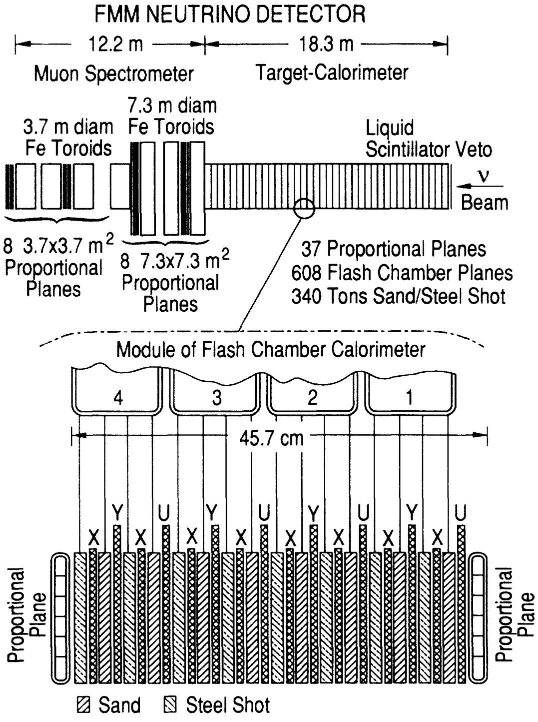

FIG. 4. General layout of the flash-chamber–proportional-tube calorimeter and details of a module. The calorimeter was about 20 m long and had a cross-sectional area of about 3.65×3.65 m^2. The flash-chamber planes alternated in an U-X-Y-X pattern, where X chambers had their cells running horizontally, U and Y chambers had their cells ±10° about the vertical direction. The proportional tube chambers were placed every 16 flash chambers with their wires is in a horizontal-vertical alternating pattern. The material of the calorimeter was sand (SiO_2) and steel shot (Fe) contained in plastic extrusions.

A typical charged-current event is shown in Fig. 5(a). This event type is distinguished by an outgoing muon track which penetrates the rear section of the calorimeter and the iron toroid system. In Fig. 5(b) we show a typical neutral-current event in which there is no such track. This event is shown on an expanded scale in Fig. 5(c). Each dot in the flash chamber calorimeter corresponds to one 5-mm×5-mm cell. The proportional tube response to the hadronic shower is displayed on the top and the bottom of Figs. 5(a) and 5(b). The event display was useful in visually scanning the events to determine the event type, measure the event vertex, and search for "exotic" interactions.

C. Event reconstruction

The ensemble of cells of the flash chamber which were struck by a hadronic shower provided a digital hit pattern of the energy deposited in the calorimeter. The total

TABLE I. The properties of the fine-grained calorimeter are given. The radiation length, interaction length, and sampling are average quantities.

Density	X_0	ΔX_0	λ	$\Delta\lambda$	Neutron excess
1.38 g/cm^3	12 cm	22.1%	85 cm	3.59%	1.94%

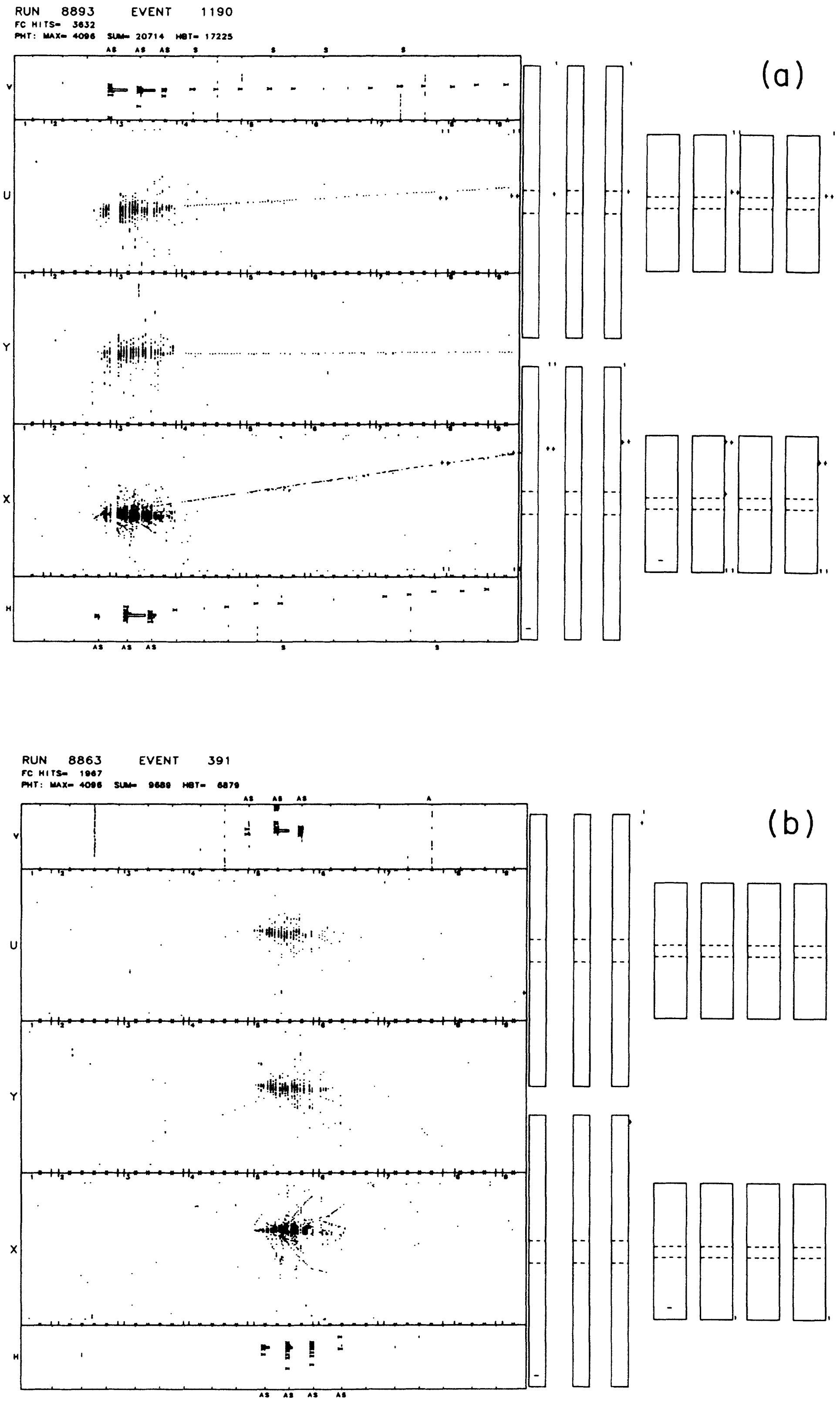

FIG. 5. (a) A typical charged-current event in the calorimeter. The event is identified by the muon emerging from the hadronic shower. Each dot in the flash-chamber display is a 5-mm × 5-mm hit cell. The energy deposition of the shower as measured by the proportional tube chambers is shown above and below the flash chamber display. (b) Typical neutral-current event. The neutral-current events were identified by the absence of a muon track emerging from the primary vertex. (c) A close-up view of the primary vertex of the neutral-current event shown in (b).

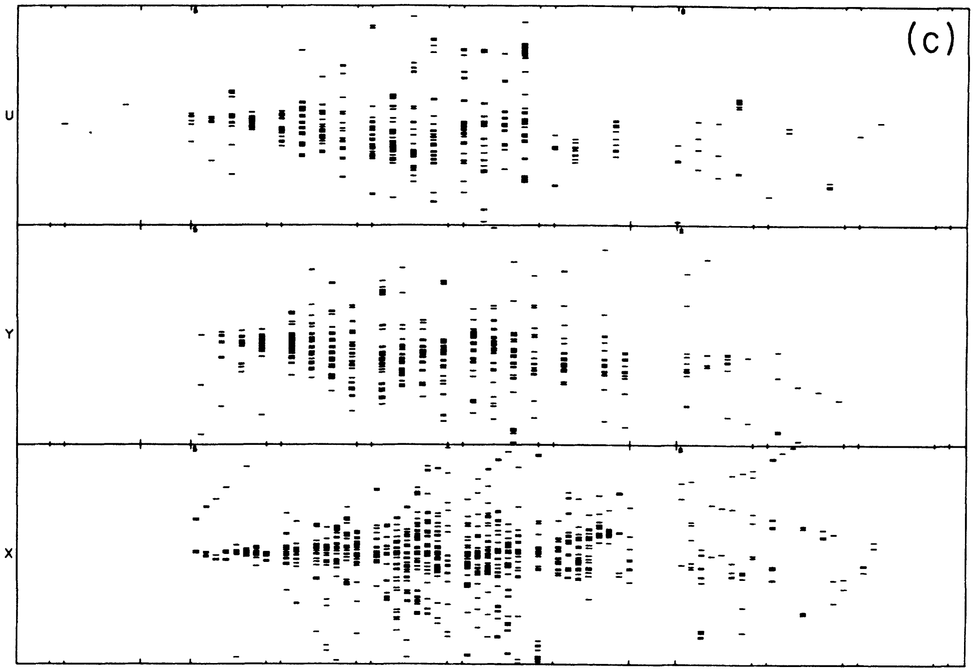

FIG. 5. (*Continued*).

number of hit cells was roughly proportional to the kinetic energy of the hadronic shower. The nonlinear energy response of the digital flash chamber calorimeter, arising from the finite lateral size of the flash chamber cells, was improved by computing the local density of hit cells throughout the spatial extent of the shower. The local density of hit cells could be statistically related to the true number of tracks which traversed a given section of the calorimeter by a simple model.[16] The residual nonlinearity was absorbed into a nonlinear calibration curve. Some pattern recognition on the showers was also performed for other analyses where electron showers from ν_μ-electron elastic scattering ($\nu_\mu e^- \rightarrow \nu_\mu e^-$) (Ref. 17) were distinguished from hadronic showers, and quasielastic ($\nu_\mu N \rightarrow \mu^- N$), and inverse-muon-decay ($\nu_\mu e^- \rightarrow \nu_e \mu^-$) events were identified.[18]

The angle of the shower was determined in two ways: (1) by fitting the center of gravity of hit cells in each chamber as a function of the shower depth and (2) by determining the centroid of the histogram of the hit cells as a function of angle measured from the primary vertex. The results given in Sec. IV A on the x dependence of the NC/CC ratio used algorithm (1), and the rest of the results involving the unfolding of the valence and sea distributions themselves used algorithm (2). The two methods of determining the hadronic shower angle gave resolutions which were nearly identical, but the behavior of algorithm (2) was more thoroughly studied on neutrino data.

Events with a recognizable muon track from the vertex were classified as charged-current events. All others were classified as neutral-current events. The detection of the outgoing muon track involved several pattern-recognition algorithms which exploited the fine-grained sampling of our detector. First, the regions of dense energy deposition were filtered out thereby enhancing isolated tracks. Second, a histogram of angles from the primary vertex of the remaining flash chamber hit cells was accumulated. If a long penetrating track was detected by observing a prominent peak in the angle histogram which survived hit density and range cuts, the event was classified as a charged-current event. The minimum muon energy which could be detected was about 1 GeV.

A semiautomated scanning station was developed around the on-line computer system. The scanning software had the capability of expanding the scale of the display so that details of an event could be more closely examined. The scanning information played a crucial role in developing and checking the computer algorithms which classified the event type and calculated the vertex position and energy of the hadronic shower.

The energy and angle responses of the calorimeter and muon spectrometer were studied on several occasions using a calibration beam of hadrons, electrons, and muons. However, it was found that this beam had a limited usefulness since the measured response of the detector in the calibration beam was somewhat different from the response during the neutrino data taking. This difference was due to an instrumental effect arising from the fact that the electron and hadron showers in the calibration beam were always absorbed in the same region in the calorimeter.

Therefore the final calibration constants for this analysis were derived from charged-current events using the hadronic shower energy spectrum and the energy-versus-radius correlation of the narrow-band beam.[1] The calibration-beam data were consistent within their systematic errors with the neutrino data calibration. The toroid magnetic field map was simultaneously determined in this calibration procedure and was found consistent with the direct magnetic field measurements.

The scaling variables x and y are related to the energy and angle of the hadronic shower, and the incident neutrino energy by the equation

$$E_h \tan^2\theta_h = 2Mx\,[(1-y-xMy/2E_\nu)/(1+xM/E_\nu)^2] \ . \tag{14}$$

Neglecting the terms M/E_ν (which were of order of 3% or less for $E_\nu > 30$ GeV) we find

$$x \approx E_h \tan^2\theta_h / 2M(1-y) \ . \tag{15}$$

The scaling variable y for neutral-current events is determined by

$$y = E_h / E_\nu(r) \ , \tag{16}$$

where E_h is the hadronic shower kinetic energy and $E_\nu(r)$ is the energy of the incident neutrino determined by the energy-versus-radius correlation of the narrow-band beam. We plot in Fig. 6 the kinematics of deep-inelastic scattering in terms of the neutral-current observables. Shown are the contours of constant x and y in terms of the observable E_h and θ_h for a fixed incident neutrino energy, $E_\nu = 50$ GeV.

D. Resolutions

Charged-current neutrino events were used to study the angle resolution by reconstructing the hadron-shower angle in the direction perpendicular to the plane formed by the incident neutrino and outgoing muon. Since the angle perpendicular to this plane had to be zero, the width of the measured angle distribution was an indication of the hadron-shower resolution. The angle resolution depended on the shower energy and the vertex position resolution, and by using charged-current data both of these experimental contributions were automatically taken into account. The data in Fig. 7 show the hadron shower angle resolution $\sigma\theta_h$ expressed as the product of the hadron energy times the resolution $E_h \sigma\theta_h$ to better display the high-energy behavior. The data points in the figure were obtained with angle algorithm (2) (described above) with flash chamber hits from the charged-current muon track removed to best simulate the neutral-current vertex resolution. Other analyses of charged-current data and hadron beam test data are also indicated in the figure. The solid line is the parametrization used in the analysis of the angle resolution in radians:

$$\sigma\theta_h = 0.0144 + 0.90/E_h \ , \tag{17}$$

where E_h is the hadron energy in GeV. The saturation of the flash chamber calorimeter and vertex-position resolution limit the angle resolution obtainable at high energy. The systematic uncertainty in the angle resolution was conservatively taken to be 10% of the resolution itself.

The average vertex resolution over the energy range of these data was determined to be about 3 cm in both the lateral and longitudinal shower directions and was only germane to the neutrino energy determination, where the radial position of the vertex in the neutrino beam was used to estimate the incident neutrino beam energy. However, the resolution of the neutrino energy was almost completely determined by the properties of the narrow-band beam. The influence of the vertex resolution on the angle resolution was taken into account by the analysis of charged-current events discussed above.

The hadron energy resolution was determined by studying the response of the neutrino detector to a cali-

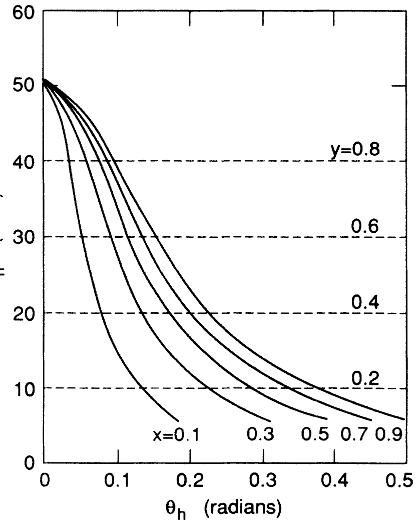

FIG. 6. The kinematics of deep-inelastic neutrino-nucleon scattering in terms of the measurables of a neutral-current event. The plot is for a fixed neutrino energy of 50 GeV. Contours of constant x and y are indicated.

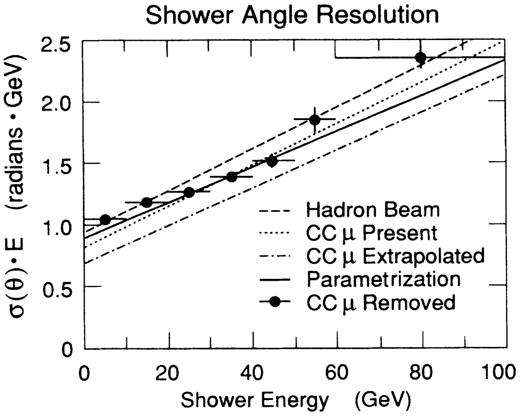

FIG. 7. The product of the hadron-shower angle resolution times the energy as a function of the hadron energy. The data were taken from an analysis of charged-current events as described in the text. The dotted line is a fit to the angle resolution times energy for charged-current events analyzed without removing the muon track from the primary vertex, the dot-dashed line is the resolution obtained by determining the vertex by extrapolating the muon, and the dashed line is the angle resolution times energy determined from hadron calibration data. The smooth line represents the fit given in the text.

bration hadron beam and was measured to be (E_h in GeV)

$$\sigma E_h/E_h = 0.05 + 0.50/\sqrt{E_h} \ . \tag{18}$$

We now study the resolution smearing of x from various experimental sources. The dependence of the x resolution on the measured hadronic energy E_h (other variables held constant) is calculated from Eq. (15) to be

$$\Delta x/x \approx [1/(1-y)]\Delta E_h/E_h \ . \tag{19}$$

Given the typical hadronic-energy resolution of 15% and the typical $y \approx 0.5$, the resulting x resolution was about 30% from this source. The incident neutrino energy contributed to the x resolution through the relation

$$\Delta x/x \approx [-y/(1-y)]\Delta E_\nu/E_\nu \ . \tag{20}$$

The typical E_ν resolution of 15% contributed a 15% x resolution at $y \approx 0.5$. The θ_h angle resolution is the controlling factor in the x resolution. From Eq. (15) the x resolution from the hadron-shower angle θ_h smearing at fixed E_ν and E_h is

$$\Delta x/x \approx (2/\cos^2\theta_h)\Delta\theta_h/\theta_h \ . \tag{21}$$

The shower-angle resolution was comparable to the shower angle itself, particularly for low-energy showers. For the typical values of $E_\nu = 50$ GeV, $x = 0.2$, and $y = 0.5$, the shower angle $\theta_h = 86$ mrad, but the angle resolution $\sigma\theta_h \approx 50$ mrad.

The resolution in y was determined by the hadronic energy resolution given above, and by the resolution in the incident narrow-band neutrino beam, which was roughly $\sigma E_\nu/E_\nu \approx 15\%$

E. Event selection

To eliminate interactions upstream of the calorimeter, the event vertex was required to be at least 8 flash chambers inside the front of the detector. Full energy containment was ensured by requiring that the vertex was at least 208 flash chambers (7.5λ) upstream of the rear end of the calorimeter and at least 50 cm (0.59λ) from the edge of the active flash chamber volume in all three views (X, Y, U). To minimize the contamination from kaon decay neutrinos, the vertex was required to be within a 100-cm radius of the neutrino beam center line. This radius cut was not used for charged-current calibration events with muons reconstructed in the spectrometer. The reconstructed hadronic energy of the events was required to be at least 10 GeV, which was well above any trigger threshold inefficiency for either charged- or neutral-current events. The hadron-shower energy was required to be less than 70% of the energy of a neutrino from pion decay at the vertex radius, that is, $y < 0.7$. This cut minimized contamination of neutral-current events from high-y charged-current events, which are characterized by difficult to recognize large-angle, low-energy muons. It also reduced the contamination from kaon decay neutrino events and avoided the kinematic region where the x resolution was poor.

Monte Carlo events with simulated hadronic showers in the detector were generated[19] and analyzed to calibrate the pattern recognition software. Care was taken in the simulation to include as much detail of the apparatus and beam as possible. Within the cuts described above, the classification algorithm misclassified approximately 4% of the neutral-current events as charged-current events and about 1% of the charged-current events as neutral-current events. The events produced by muon neutrinos from $K_{\mu 2}$ ($K_{\mu 3}$) decay were 11% (0.5%) of the neutral-current $\pi_{\mu 2}$ events after cuts. The charged-current events produced by electron neutrinos from K_{e3} decay, which had no muons and thus were classified as neutral-current events, were 1% of the accepted neutral-current event sample. The wideband neutrino background from meson decay before momentum selection in the pion-kaon beam was about 1% of the neutral-current and charged-current $\pi_{\mu 2}$ samples.

Table II summarizes the event statistics as the analysis proceeded through the stages discussed above.

TABLE II. The number of events satisfying the experimental cuts at each of the four beam conditions of the experiment are tabulated. The beam energies have been given a sign to indicate neutrinos (+) or antineutrinos (−). The details of the energy and fiducial cuts are explained in the text. The numbers in the "Experimental" row refer to events before the event misclassification correction had been applied, and the numbers in the "Corrected" row to the events after the misclassification correction.

Beam setting	−165 GeV	+165 GeV	+200 GeV	+250 GeV
Triggers	44 263	33 510	26 768	34 110
Vertex contained	15 318	18 962	13 566	15 493
Correct scan class	9098	15 877	10 336	11 324
Full reconstruction	7831	13 613	8929	9663
In Z fiducial cut	6163	10 812	7077	7624
In r fiducial cut	4933	8602	5768	6094
$E_h > 10$ GeV	3527	7224	5048	5404
$y < 0.7$	2588	4134	2754	2705
Experimental				
Charged currents	1882	3167	2126	2041
Neutral currents	706	967	628	664
Corrected				
Charged currents	1865	3148	2116	2029
Neutral currents	723	986	638	676

IV. DATA ANALYSIS

The data were analyzed in three different ways: (1) parametric fits to the ratio of the uncorrected neutral-current to charged-current x distributions, (2) parametric fits to the fully corrected and separated valence and sea quark x distributions for both interactions, and (3) a model-independent deconvolution of the valence- and sea-quark distributions for the two interactions.

A. The ratio comparison

Our comparison of the neutral-current (NC) with the charged-current (CC) x distribution began by taking the ratio of the two x distributions without performing the x-resolution unsmearing correction. This method was employed in our earlier paper[2] on this subject. The virtue of such a comparison is that it was direct and therefore the subtleties of the unsmearing correction were circumvented. Here we review this earlier result.

The comparison of the neutral-current and the charged-current x distributions is shown in Fig. 8. To reduce the systematic errors, the scaling variable x for both neutral-current and charged-current events was computed from the measured hadron recoil energy, the hadron-shower angle with respect to the incident-neutrino-beam axis, and the inferred $\pi_{\mu 2}$ neutrino energy derived from the measured vertex radius and the simulated properties of the narrow-band beam. No correction was applied for the resolution smearing, but the data were corrected for the event-type misclassification (including K_{e3} charged-current events). The charged-current data have been normalized in the figure to the number of neutral-current events at each of the secondary beam settings to make the comparison of the distributions more direct. We see that the x distributions of the two interactions agree within statistical errors.

To examine the two distributions more closely we show in Fig. 9 the NC/CC ratios for neutrinos and antineutrinos as functions of x. We combined all of the neutrino energy settings in Fig. 9(a) since there appeared to be no systematic differences among the various data sets. The bin at the highest-x value included data for reconstructed $x > 1$.

To make a quantitative comparison of the nucleon structure functions of the two interactions, we fitted the x dependence of the NC/CC ratios of both the neutrino and the antineutrino data simultaneously to determine the shape of the neutral-current structure functions *relative* to those of the charged current by the means of a simple parametric fit. The structure functions were divided into valence quarks and sea quarks. By "valence-

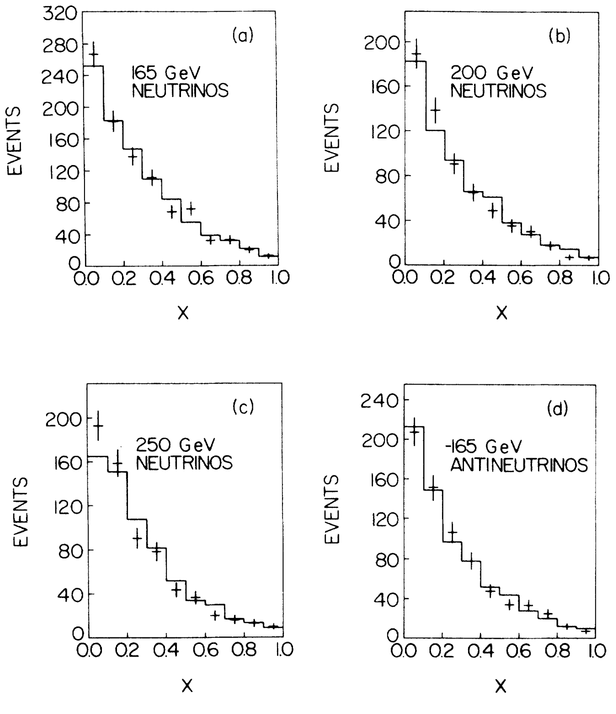

FIG. 8. Comparison of the experimental x distributions for neutral-current and charged-current events at each of the beam settings of the experiment. The points with error bars are the neutral-current data and the histograms denote the charged-current data. The charged-current distributions have been normalized to the integrals of the neutral-current distributions to make the comparison of the shapes more direct. The resolution smearing has not been corrected in these plots.

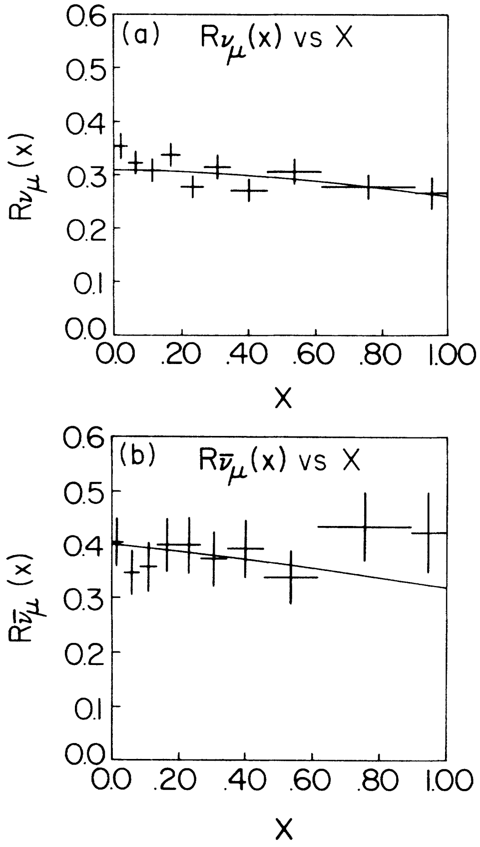

FIG. 9. (a) The neutrino NC/CC ratio as a function of x. All three neutrino beam settings have been combined in neutrino comparison. (b) The antineutrino NC/CC ratio. The lines are the overlayed fits of the neutral-current structure functions relative to those of the charged-current given in Table III. Since there was no significant difference between Fits 1 and 2, only one fit line is shown.

quark distribution" we mean the sum of the valence up- and down-quark distributions of the nucleon, which in our nearly isoscalar target had almost equal contributions from protons and neutrons. By the "sea-quark distribution" we mean the sum of antiquarks and an equal number of quarks, with a small fraction of the sea being comprised of strange quarks and strange antiquarks.

A simple parametrization of the structure functions was chosen for both the neutral-current and the charged-current interactions. It gave an adequate representation of the world's charged-current data[20,21] at our mean $Q^2=11$ (GeV/c)^2. (In terms of the standard model, the Q^2 evolution of the valence and sea structure functions should be the same for the two neutrino-nucleon interactions.) The forms of the valence and sea structure functions are given by

$$xV(x)=xq(x)-x\bar{q}(x)=Ax^{\alpha}(1-x)^{\beta}\ , \tag{22a}$$

$$xS(x)=2x\bar{q}(x)=C(1-x)^{\gamma}\ , \tag{22b}$$

where A, C, α, β, and γ are constants. Note that we have taken the sea quarks to be equal to the sea antiquarks. The charm-quark sea was neglected and the strange quark was assumed to be 20% of the total quark sea, $2x\bar{q}(x)$, consistent with measurements of this quantity.[22-24] The charged-current Monte Carlo simulation included the full Kobayashi-Maskawa[8] quark-mixing matrix, and the charm-quark kinematic threshold factor (the so-called slow-rescaling correction) where the charm-quark mass[25] was taken to be 1.5 GeV/c^2. Radiative effects[26,27] were included in the charged-current simulation.

The ratio test had little sensitivity to the shape of the neutral-current sea-quark term, and so we fixed $\gamma_{\rm NC}=\gamma_{\rm CC}=7$ in agreement with charged-current data at our mean Q^2 and in conformity with counting rule arguments.[28] We fixed $\sin^2\theta_W$ to the value determined by a one-parameter fit to the integral NC/CC ratios for neutrinos and antineutrinos.[29] (See Sec. IV G of this paper for further discussion.) Two fits of the NC/CC ratios (for neutrinos and antineutrinos) under different assumptions were performed. The fits matched a Monte Carlo simulation of the experiment with the data and included all of the known experimental resolution smearing effects. In Fit 1, the values of the A, β, and C were determined under the constraint $\alpha=\frac{1}{2}$ in accordance with the charged-current data[20,21] and the prediction of Regge theory.[30] The results of Fit 1, which do not depend on the assumptions of the Gross-Llewellyn Smith (GLS) sum rule,[7] were consistent with the sum rule prediction. In Fit 2 we included the GLS sum-rule constraint and fit for α, β, and C thereby testing the self-consistency of our procedure.

The results of the fits are shown in Table III. Instead of tabulating the sea strength parameter C, we quantified the magnitude of the quark sea by the ratio

$$Z=\bar{Q}/(Q+\bar{Q})\ , \tag{22c}$$

where $Q=\int xq(x)dx=\int[xV(x)+\frac{1}{2}xS(x)]dx$ and $\bar{Q}=\int x\bar{q}(x)dx$. It is important to note that only the differences between the assumed values of the charged-current parameters and the determined neutral-current parameters are significant. By this ratio comparison we determined the neutral-current structure functions relative to those of the charged-current interaction. The fits indicated the neutral-current and the charged-current parameters agree to within one standard deviation.

In estimating the systematic errors of the fits we considered the sensitivities to different values of $\sin^2\theta_W$, the hadronic energy scale, the event classification, and the upper y cut. Systematic errors from the uncertainties of the strange sea, the slow-rescaling threshold, the radiative corrections, and the Kobayashi-Maskawa matrix were included, although they were smaller than the errors from the experimental sources listed above.

B. Method of extraction of quark distributions

The ratio test did not actually separate the neutral-current valence and sea distributions nor did it allow the neutral and charged-current distributions to be analyzed separately. Hence we performed separate full deconvolutions of the neutral-current and charged-current structure functions. The goal of this analysis was to extract the valence- and sea-quark distributions on a bin-by-bin

TABLE III. The ratio comparison of the neutral-current (NC) structure functions with those of the charged current (CC) is given. The first error for each neutral-current parameter is the statistical error determined by the fitting procedure, and the second error is an estimate of the systematic error. The entries with no error are the input parameters. The fit parameters are defined in Eq. (22). $N_{\rm DF}$ denotes the number of degrees of freedom.

		Fit 1	Fit 2
Parameter	CC	NC	NC
Valence			
A	3.28	3.59±0.63±0.62	$A=3\Gamma(\alpha+\beta+1)/\Gamma(\alpha)\Gamma(\beta+1)$
α	0.5	0.5	0.48±0.10±0.10
β	3.0	3.54±0.40±0.41	3.38±0.62±0.54
Sea			
Z	0.137	0.161±0.038±0.03	0.169±0.038±0.03
γ	7.0	7.0	7.0
$\int_0^1 V(x)dx$		3.1±0.5	
$\chi^2/N_{\rm DF}$		32.0/37	32.0/37

basis, fully corrected for all the experimental conditions.

The dependence of the structure functions on valence and sea quarks for neutral currents [Eqs. (9) and (10)] differs from that of charged currents [Eqs. (6)–(8)]. Therefore we chose to present our results as quark distributions to facilitate a more direct comparison between charged and neutral currents. Resolutions in x and Q^2 for a neutral-current analysis are worse than for a conventional charged-current analysis, primarily because shower angle resolution is worse than muon angle resolution. We therefore chose to bin our data only in x and not also in Q^2.

The conventional method of separating F_2 and xF_3, or equivalently the valence quarks, sea quarks, and antiquarks, is by sums and differences of neutrino and antineutrino data. The antiquark distribution requires subtraction and is limited by the statistics of the smaller of the data sets. However, there is also information about the quark and antiquark content in the shape of the y distribution if the Q^2 evolution of the x distributions is known. This y information allows quark and antiquark distributions to be separated using neutrino data alone with no antineutrino data, or vice versa. Using the Q^2 evolution measured by other experiments, we could exploit our y distribution to obtain a better separation of the valence quarks, sea quarks, and antiquarks than by the difference method alone.

The poor x resolution inherent in a neutral-current analysis required special attention to the resolution corrections. The basis of our technique was to summarize the experimental resolution in a matrix **A**. The element A_{ij} represented the probability of an event from the true x bin j to reconstruct into data bin i. If x_j is the number of events in the true x bin labeled by the index j, and b_i is the number of events in the data bin labeled by i, then

$$\sum A_{ij}x_j=b_i \ . \tag{23}$$

Note that repeated indices imply summation.

The binning of the true distribution and the data need not be the same, and we employed more bins for the data than for the true distribution. The true x distribution that best fits the data was found by minimizing the χ^2 defined by

$$\chi^2=\sum \left[b_i-\sum_j A_{ij}x_j\right]^2 \Big/ \sigma_i^2 \ , \tag{24}$$

where σ_i^2 were the statistical variances of the data bins, b_i. The χ^2 minimization problem reduced to solving

$$\sum W_{jk}x_j=R_k \ , \tag{25}$$

where

$$W_{jk}=\sum A_{ij}A_{ik}/\sigma_i^2 \tag{26a}$$

and

$$R_k=\sum b_i A_{ik}/\sigma_i^2 \ . \tag{26b}$$

Note that the **W** matrix contains the resolution smearing information and the statistical errors of the data, and the vector **R** contains the data information. The statistical errors of the resolution-corrected distribution were obtained from the inverse of **W**.

The matrix formalism was sufficiently general to perform all the steps of extracting the quark distributions. The solution vector **x** was generalized to have both valence and sea components for each bin. The data vector **b** was generalized to contain all the information from the experiment: the three-dimensional distribution in reconstructed x, reconstructed y, and vertex radius (corresponding to neutrino energy) at each of the neutrino beam settings. It is important to emphasize that the smearing matrix **A** depended on the detector resolution and on the physics relating the x distribution to the cross section, but not on the x distribution itself.

The **A** matrix was calculated by Monte Carlo simulation of the full standard-model physics of deep-inelastic scattering, the neutrino beam, the detector resolution, and the data selection rules. To simplify the structure function model, the Callan-Gross relation[11,31] for both the neutral-current and the charged-current structure functions was assumed. The effects of the target neutron excess, the strange sea, Kobayashi-Maskawa mixing, slow rescaling of charm production, and radiative corrections to the total cross sections and to charged-current kinematics were included.

The Monte Carlo calculation of the **A** matrix included a parametrization of the Q^2 evolution of the valence- and sea-quark distributions. Our extracted distributions are therefore implicitly corrected to $Q^2=10$ (GeV/c)^2 which is close to the mean value of 12 and 8 (GeV/c)^2 for our neutrino and antineutrino data, respectively. The corrections are given by power-law dependences[1]:

$$xV(x,Q^2)=xV(x,Q_0^2)(Q^2/Q_0^2)^{p_v(x)} \ , \tag{27a}$$

$$xS(x,Q^2)=xS(x,Q_0^2)(Q^2/Q_0^2)^{p_s(x)} \ , \tag{27b}$$

where $Q_0^2=10$ (GeV/c)^2, and the functions $p^{v,s}(x)=p_0^{v,s}(1-x/p_c^{v,s})$ (indices v and s correspond to the valence and sea, respectively), are independent of Q^2 with $p_0^v=0.132$, $p_c^v=0.210$, $p_0^s=0.265$, and $p_c^s=0.115$. This Q^2 evolution was derived from a fit to the Chicago-Columbia-Fermilab-Rochester-Rockefeller[20] (CCFRR) and the CERN-Dortmund-Heidelberg-Saclay-Warsaw[21] (CDHSW) Collaborations charged-current structure-function data. The parametrization was in good agreement with the parametrization of Duke and Owens[32] from $Q^2=0.1$ (GeV/c)^2 to $Q^2=200$ (GeV/c)^2. We used the latter parametrization in our earlier analysis.[2] The Q^2 dependence of the gauge-boson propagator was considered and found to be negligible.

A submatrix was calculated for each beam setting, and the submatrices for the different beam settings were combined. The charged- and neutral-current data were analyzed independently. Misclassification of event type was Monte Carlo simulated and included in each analysis. Since the bin populations were rather small, a Poisson maximum-likelihood formalism was used rather than the Gaussian χ^2 formalism derived above. For each beam setting, the submatrix was normalized such that the number of accepted charged-current events predicted for the quark distributions assumed in the Monte Carlo simulation was equal to the number of accepted charged-current events in the data. The charged-current total cross section was constrained to that of Ref. 33, thus constraining the integrals, but not the shapes, of the extracted charged-current distributions. The same normalization factor was then used for neutral-current events in conjunction with a value for $\sin^2\theta_{W'}$ which we set to 0.238, derived from a fit to our neutrino data (see Sec. IV G).

C. Parametric fits to the quark distributions

We performed parametric fits of the structure functions using the full **W** matrix by minimizing the χ^2 as a function of the quark distribution parameters. The variation of χ^2 around its minimum value may be written

$$\delta\chi^2(\alpha,\beta,\ldots)=\sum \delta x_i\, W_{ij}\delta x_j \ , \tag{28}$$

where $\delta x_i=[x_i(\alpha,\beta,\ldots)-x_i^*],x_i^*$ is the ith bin of the quark distribution which minimizes χ^2 found by the solution of Eq. (23), $x_i(\alpha,\beta,\ldots)$ is the ith bin of the parametrization, and $\alpha,\beta,\ldots$ are the quark distribution parameters. Once the **W** matrix and the solution vector $\mathbf{x}^*$ was determined, this second χ^2 minimization was a relatively easy problem to solve.

The quark valence and sea x distributions were taken to be simple functional forms where the valence-quark distribution was parametrized by Eq. (22a) and the sea by Eq. (22b). The poor x resolution of the data, propagated through the unfolded solution, made a simultaneous fit of all of the parameters of Eq. (22) unfeasible. Thus we followed the spirit of the ratio test described above. For the first determination of the structure function parameters we fixed $\alpha=0.5$ and determined the valence magnitude parameter A and the shape parameter β. In the second fit we assumed that the Gross–Llewellyn Smith (GLS) sum rule[34] was satisfied by demanding that $\int_0^1 V(x)dx=3$, and determined the valence shape parameters α and β. The GLS sum rule implies that the constants A, α, and β satisfy the relation $A=3\Gamma(\alpha+\beta+1)/\Gamma(\alpha)\Gamma(\beta+1)$. For the sea, $\gamma=7$ was assumed, and only the normalization of the sea controlled by the parameter C was determined. Since the value of C and γ were correlated, the result was quoted in terms of the parameter Z defined in Eq. (22c).

The results of the fits are shown in Table IV. We note that the neutral-current structure function parameters agree with those of the charged current. The charged-current parameters agree with other charged-current data within the systematic errors of the deconvolution process to be discussed below. These results are in essential agreement with ratio test discussed above (see Table III).

Note that the valence parameters A, α, and β are highly correlated in the fit: an excursion of any one parameter by one standard deviation caused the others to change by almost one unit of their standard deviations. The Z parameter, which measured the magnitude of the sea, is also correlated with the valence parameters. The quoted errors are the extreme changes in each parameter letting all other parameters float to minimize the χ^2 of the fit.

Several sources of systematic errors were considered in the fits. The most important sources were energy and angle scale errors which affect the scale of the x distribution, and the hadron angle resolution. If the reconstructed x value of each event were reduced by 5% the neutral-current parameters of the GLS constrained fit changed in the following way: $\Delta\alpha=0.07$, $\Delta\beta=0.63$, and $\Delta Z=0.007$. Comparable changes were observed in the charged-current parameters. Degrading the angle resolution in the **A**-matrix calculation by 10% changed the GLS parameters of the neutral-current fit by $\Delta\alpha=0.23$, $\Delta\beta=1.8$, and $\Delta Z=0.001$. Smaller changes in the corresponding charged-current parameters were observed. These changes of the fit parameters α and β are roughly a factor of 3 larger than the statistical errors of the neutral-current fits.

TABLE IV. Tabulated are parameters of fits to the extracted NC and CC quark distributions. Fit 1 in the table corresponds to the simultaneous determination of A, β, and Z with the parameter $\alpha=0.5$. Fit 2 is the GLS-constrained fit where α, β, and Z are determined. The χ^2/N_{DF} is the χ^2 divided by the number of degrees of freedom of the fits. All errors are from statistical sources. The quantity (A) shown in Fit 2 is derived from the values of the other fit parameters.

Fit 1 Constraint $\alpha=0.5$	NC	CC
A	3.108 ± 0.444	2.784 ± 0.171
β	2.658 ± 0.253	2.175 ± 0.102
Z	0.174 ± 0.022	0.134 ± 0.0098
$\int_0^1 V(x)dx$	3.0 ± 0.5	2.9 ± 0.3
χ^2/N_{DF}	42.08/21	32.94/21
Fit 2 Constraint GLS sum rule $A=3\Gamma(\alpha+\beta+1)/\Gamma(\alpha)\Gamma(\beta+1)$		
(A)	(3.159)	(2.872)
α	0.502 ± 0.080	0.494 ± 0.035
β	2.681 ± 0.414	2.230 ± 0.167
Z	0.172 ± 0.019	0.128 ± 0.0093
χ^2/N_{DF}	42.09/21	33.73/21

D. Eigenvector analysis

It was desirable to go beyond parameter fits and perform a parameter-free analysis of the neutral-current quark distribution. This was possible by exploiting more fully the information in the **W** matrix. The general strategy was to find the eigenvectors of the **W** matrix and expand the neutral-current quark distributions in terms of these eigenvectors.

The **W** matrix was diagonalized by finding a unitary matrix **U** and a diagonal matrix **Λ** such that $\mathbf{W}=\mathbf{U}^{-1}\mathbf{\Lambda}\mathbf{U}$. The columns of **U** were the eigenvectors of **W**, and the diagonal elements of **Λ** were the corresponding eigenvectors, $\lambda_k=\Lambda_{kk}$. **W** could always be diagonalized with all the eigenvalues λ_k positive, since it was constructed from χ^2, which is positive definite.

We can view the eigenvectors and eigenvalues of the **W** matrix as providing a natural sequence of orthonormal functions. The functions are the eigenvectors, and the order is provided by the eigenvalues. This suggests that we can express the solution $\mathbf{x}^*$ of the minimum-χ^2 problem as a linear combination of the eigenvectors:

$$x_k^*=\sum U_{kn}c_n \ , \tag{29}$$

where $c_n=\sum x_k^* U_{nk}^{-1}$.

We rewrite the variation of χ^2 around the minimum for an error vector $\boldsymbol{\delta}\mathbf{x}$ using the diagonalized form of the **W** matrix as

$$\delta\chi^2=\sum \delta x_m U_{mi}^{-1}\Lambda_{ij}U_{jn}\delta x_n \ . \tag{30}$$

The projection of the error vector on the kth eigenvector was defined as

$$\delta c_k=\sum U_{kn}\delta x_n=\sum \delta x_m U^{-1}mk \ . \tag{31}$$

The change of χ^2 is then written as a one-dimensional sum:

$$\delta\chi^2=\sum \lambda_k(\delta c_k)^2 \ . \tag{32}$$

Thus each eigenvector has an independent contribution to the χ^2. The eigenvectors with large eigenvalues have a large influence on the χ^2, and those with small eigenvalues have a small influence. The statistical errors of the coefficients c_k are related to the eigenvalues:

$$\sigma c_n=\lambda_n^{-1/2} \ . \tag{33}$$

The first eigenvectors in the sequence will have expansion coefficients with small errors, and later eigenvectors will have increasingly larger errors. At some point in the sequence we expect the errors on the coefficients to exceed the coefficients themselves. If we simply set their coefficients to zero we eliminate statistical noise from the solution at insignificant cost to the χ^2, or to the information of the eigenvector expansion.

E. Eigenvector-analysis results

We performed separate eigenvector analyses on our neutral- and charged-current quark distributions. The full solutions were expanded as linear combinations of the eigenvectors of the **W** matrices, where each interaction had its own set of eigenvectors sorted by its eigenvalues. Our rule was to truncate the expansion at the point when both of the next two consecutive eigenvector contributions improved the χ^2 by less than one unit. This required four eigenvectors for the charged-current data, and only one for the neutral currents, although four were retained in the analysis for consistency with the charged currents. In Figs. 10 and 11 the first four eigenvectors of the neutral-current and charged-current deconvolutions properly normalized by the expansion coefficients c_k are shown. The normalized quark valence $xV(x)$; sea $xS(x)$; and the sum of the valence and sea eigenvectors are all indicated in the figures. The convoluted solution was obtained by summing the eigenvectors as shown. As an indicator of the progression of the eigenvector expansion we computed $\Delta\chi^2=\chi_{i-1}^2-\chi_i^2$, where the index i denoted the order of the eigenvector. For the $\Delta\chi^2$ value computed for the first eigenvector, χ_0^2 was evaluated by assuming that the structure function was zero.

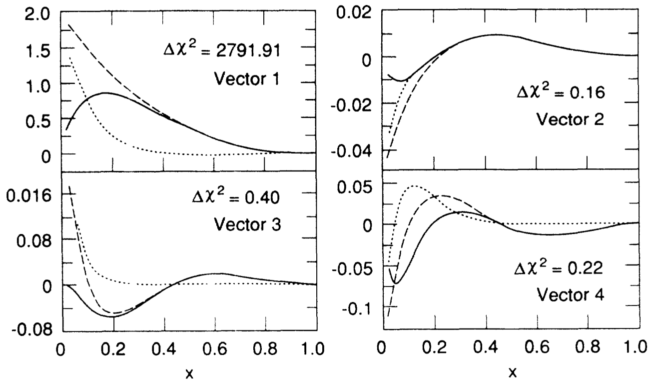

FIG. 10. The first four eigenvectors of the extracted neutral-current quark distributions. The valence functions $xV(x)$ are indicated by solid lines; the sea $xS(x)$ by dotted lines; and $F_2(x)=xV(x)+xS(x)$ by dashed lines. The $\Delta\chi^2$ value (defined in the text) from each eigenvector is shown. Note that the higher-order eigenvectors oscillate as a function of x and contribute less than the lower-order eigenvectors.

Figures 12 and 13 show the cumulative sums of the eigenvector contributions. The error bars are the statisti-

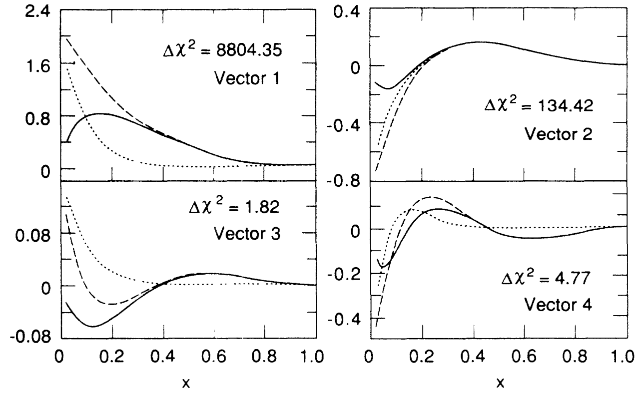

FIG. 11. The first four eigenvectors of the charged-current quark distributions. The solid, dotted, and dashed lines follow the same convention as Fig. 10.

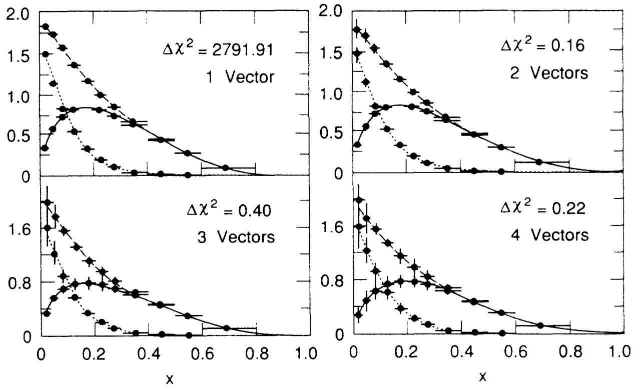

FIG. 12. The eigenvector expansion for the neutral-current interaction is shown as a function of the number of contributing eigenvectors. The solid, dotted, and dashed lines follow the same convention as Fig. 10.

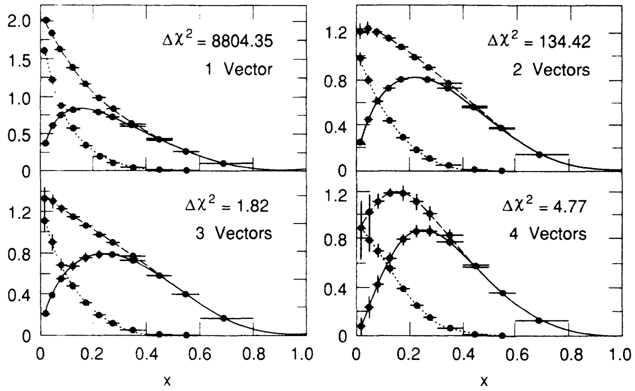

FIG. 13. The eigenvector expansion for the charged-current interaction. The solid, dotted, and dashed lines follow the same convention as Fig. 10.

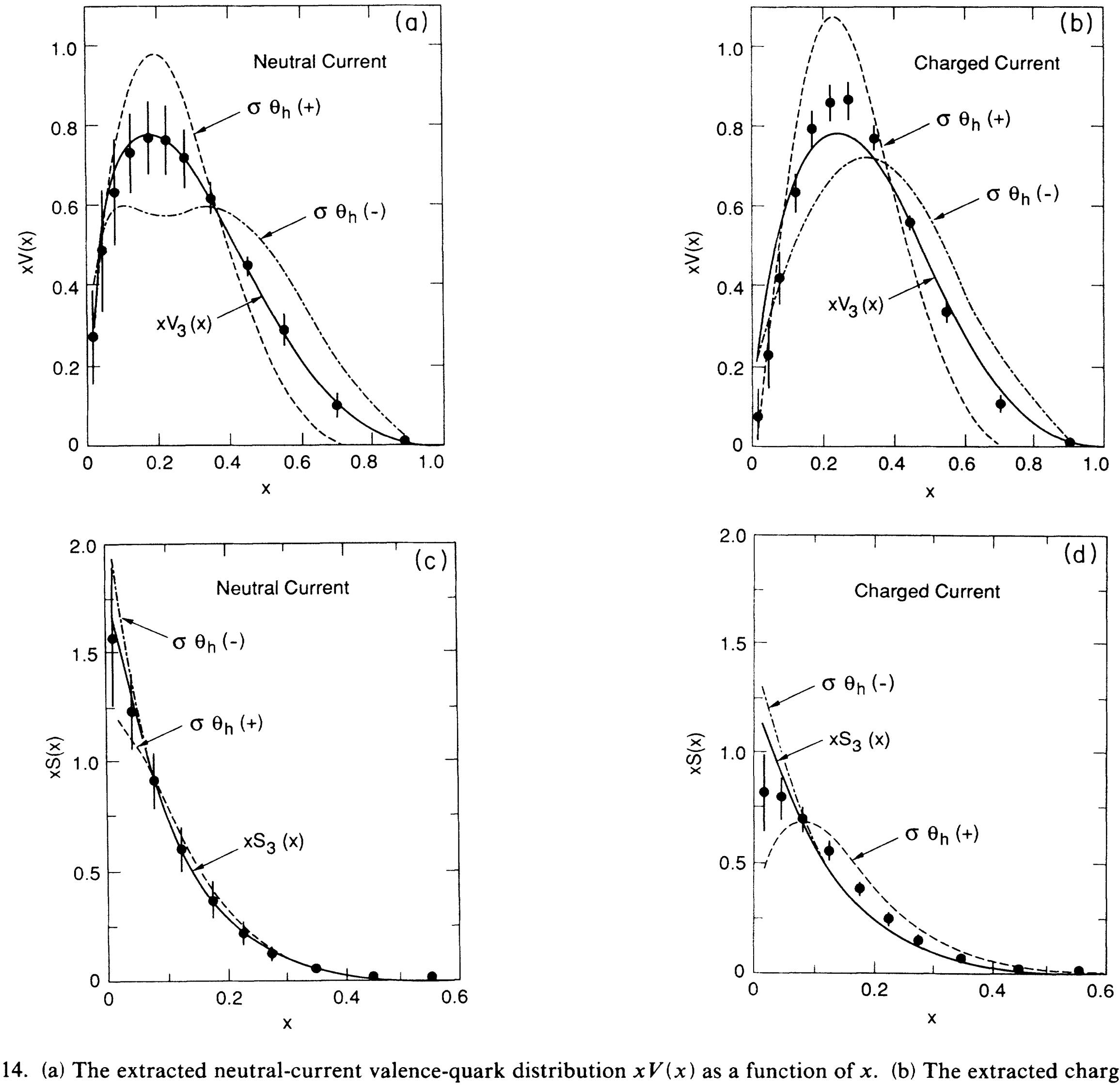

FIG. 14. (a) The extracted neutral-current valence-quark distribution $xV(x)$ as a function of x. (b) The extracted charged-current valence-quark distribution. (c) The extracted sea-quark distribution $xS(x)$ for the neutral-current interaction. (d) The extracted sea-quark distribution for the charged-current interaction. As discussed in the text, the distributions are referenced to $Q^2=10\ (\text{GeV}/c)^2$. The dotted and dashed lines indicate the effect of changing the hadronic-shower angle resolution by ±10% in the deconvolution, and the solid line shows the distribution obtained by adding only the first three eigenvectors of the eigenvector expansion. The error flags indicate the statistical errors determined from the first four eigenvectors.

cal errors of the expansion coefficients propagated to the summed distributions. While the errors of the expansion coefficients are uncorrelated, the errors on the bins of the truncated sums remain correlated. In particular, the fourth eigenvector of the charged currents has a significance of only about 2σ, but changes every bin by roughly 2σ in a correlated way.

The deconvoluted valence distributions calculated from the sum of the first four eigenvectors for the neutral-current and the charged-current interaction are shown in more detail in Figs. 14(a) and 14(b), respectively. Figures 14(c) and 14(d) show the respective quark sea distributions. To indicate the eigenvector expansion sensitivity to our cutoff criterion discussed above, the eigenvector expansion as determined from the first three eigenvectors is shown as the solid line. We checked that the parametric fits to the four-eigenvector sum gave the same result within errors as the fits to the complete data providing confidence that the four eigenvector sums shown in Fig. 14 contained essentially all of the information of the deconvoluted structure functions. We reached a similar conclusion when we noted that the χ^2 values of the eigenvector expansion were saturated by this partial sum.

The largest systematic uncertainty in the result was due to the uncertainty in the x resolution, which was dominated by the shower-angle resolution. The analysis was therefore repeated with **A** matrices corresponding to 10% better and worse angle resolutions. The resulting systematic errors are indicated by the broken lines in Fig. 14. Another uncertainty was the x scale, with contributions from the shower-energy, shower-angle, and neutrino-energy scales. The sensitivity to the x scale was determined by repeating the analysis with reconstructed x of each event reduced by 5%. Tables V and VI show the deconvoluted neutral-current valence and sea distributions, and Tables VII and VIII the corresponding distributions for the charged currents. The systematic errors discussed above are also tabulated.

F. Comparisons with CHARM

The CERN-Hamburg-Amsterdam-Rome-Moscow (CHARM) Collaboration reported results of the deconvoluted structure functions for the neutral-current and the charged-current interactions from a high-statistics exposure to the 160-GeV/c narrow-band beam at CERN.[35] Their neutrino detector was a fine-grained calorimeter mounted in front of an iron spectrometer with a toroidal magnetic field, and surrounded by magnetized iron frame. The experiment recorded roughly 31 000 neutral-current neutrino events, and 1900 neutral-current antineutrino events.

The experimental x resolution smearing was deconvoluted by the statistical unfolding method of Blobel.[36] The CHARM Collaboration employed cubic spline functions which were "regularized" to damp the noise oscillations inherent in the deconvolution process instead of truncating the eigenvector expansion at the point where the χ^2 value is saturated, as we did.

They reported their results in terms of the $F_\pm$ structure functions and the antiquark sea. The $F_+(x)$ [$F_-(x)$] structure function corresponds to neutrino- [antineutrino-] nucleon scattering. The cross section for neutrino-nucleon scattering integrated over y is given by

$$d\sigma_\nu/dx=(G_F^2 M E_\nu/2\pi)F_+(x) \; . \tag{34}$$

The structure functions $F_\pm(x)$ will therefore be combinations of the valence and sea distributions and in the neutral-current case will also depend on $\sin^2\theta_W$. If the small strange and charm sea quark terms are neglected we find, for the neutral-current case,

$$F_+(x)=(2g_L^2+\tfrac{2}{3}g_R^2)xV(x)+\tfrac{4}{3}(g_L^2+g_R^2)xS(x) \; , \tag{35a}$$

$$F_-(x)=(\tfrac{2}{3}g_L^2+2g_R^2)xV(x)+\tfrac{4}{3}(g_L^2+g_R^2)xS(x) \; , \tag{35b}$$

where $g_L^2=(u_L^2+d_L^2)$ and $g_R^2=(u_R^2+d_R^2)$.

TABLE V. The extracted neutral-current valence-quark distribution referenced to $Q^2=10$ (GeV/c)^2 is tabulated as a function of x. The columns are as follows: "x bin" is the central value of the x bin, $xV_{\rm NC}(x)$ is the neutral-current valence-quark structure function evaluated from the sum of the first four eigenvectors, $\sigma_{\rm stat}$ is the associated statistical error. The systematic errors are given by $\Delta[\sigma\theta_h(+)]$, the difference between the neutral-current valence-quark distribution deconvoluted with the hadronic-shower-angle resolution degraded by 10% and the central value $xV_{\rm NC}(x)$; $\Delta[\sigma\theta_h(-)]$, the corresponding difference with the hadronic-shower-angle resolution improved by 10%; $\Delta_{\rm scale}$ is the change if the data are analyzed with all reconstructed x values reduced by 5%.

x bin	$xV_{\rm NC}(x)$	$\sigma_{\rm stat}$	$\Delta[\sigma\theta_h(+)]$	$\Delta[\sigma\theta_h(-)]$	$\Delta_{\rm scale}$
0.015	0.2712	0.1208	−0.0251	0.094	0.0424
0.045	0.4856	0.1579	0.0157	0.0696	0.0747
0.080	0.6317	0.1372	0.0942	−0.0304	0.0929
0.125	0.7318	0.1039	0.1796	−0.1361	0.0974
0.175	0.7735	0.0928	0.2083	−0.1936	0.0819
0.225	0.7668	0.0907	0.1928	−0.1923	0.0561
0.275	0.7221	0.0794	0.1300	−0.1337	0.0248
0.350	0.6224	0.0491	0.0219	−0.0250	−0.0204
0.450	0.4534	0.0253	−0.1123	0.1009	−0.0551
0.550	0.2899	0.0429	−0.1651	0.1559	−0.0645
0.700	0.1028	0.0327	−0.1103	0.0981	−0.0350
0.900	0.0050	0.0029	−0.0087	0.0074	−0.0026

TABLE VI. The extracted neutral-current sea-quark distribution referenced to $Q^2=10$ (GeV/c)^2 is tabulated as a function of x. The columns are defined with the same conventions as in Table V.

x bin	$xS_{\mathrm{NC}}(x)$	σ_{stat}	$\Delta[\sigma\theta_h(+)]$	$\Delta[\sigma\theta_h(-)]$	Δ_{scale}
0.015	1.579	0.3080	−0.3460	0.385	0.0097
0.045	1.241	0.1784	−0.1320	0.103	0.0135
0.080	0.9218	0.1300	−0.0076	−0.0548	0.0119
0.125	0.6076	0.1074	0.0541	−0.1016	0.0061
0.175	0.3704	0.0795	0.0472	−0.0831	−0.0015
0.225	0.2188	0.0525	0.0295	−0.0512	−0.0051
0.275	0.1236	0.0307	0.0112	−0.0230	−0.0063
0.350	0.0486	0.0117	0.0001	−0.0043	−0.0047
0.450	0.0116	0.0025	−0.0024	0.0014	−0.0019
0.550	0.0021	0.0004	−0.0010	0.0008	−0.0005

We compare the $F_{\pm}(x)$ structure functions of the two experiments in Figs. 15 and the antiquark distributions in Fig. 16. Both data sets were referenced to $Q^2=10$ (GeV/c)^2. (Note that the CHARM Collaboration derived the antiquark distribution by a linear combination of F_+ and F_-, rather than utilizing the y distribution as our analysis does.) We conclude that the two experiments are in agreement within their respective statistical and systematic errors.

The CHARM Collaboration also has performed parametric fits to the valence and sea structure functions of the neutral-current and the charged-current interactions. As in our experiment they found that the quark distributions in the nucleon for the two interactions are the same within errors.

G. Determination of $\sin^2\theta_W$ and ρ

In an earlier paper[29] we determined both $\sin^2\theta_W$ and ρ, the parameters describing the relative strength of the neutral-current quark-Z^0 coupling with respect to the charged-current quark-$W^{\pm}$ interaction in the standard model. Here we update our determination of these parameters including some small and subtle factors neglected in our earlier paper. The previous analysis did not account for the QCD Q^2 evolution of the structure functions below $Q^2=4$ (GeV/c)^2, and neglected the small nonisoscalar target correction. The correction of hadron shower energies for contamination from muon energy has been improved, and the effect of event misclassification on the event energy has been taken more fully into account. All of these effects tended to lower the value of $\sin^2\theta_W$. This new result, which is more complete than the previous one, is nevertheless within the quoted systematic error of the previous result.

Several methods of extracting $\sin^2\theta_W$ have been discussed. The Paschos-Wolfenstein method[37] or the Llewellyn Smith formula[38] are among the more commonly used techniques. Each method has its own advantages, and both methods address the problem of how to correct for the small, but important antiquark terms in the neutral-current and the charged-current cross sections. Both methods require either the relative normalization of the neutrino and antineutrino cross sections or the relative neutrino and antineutrino fluxes be known. The methods are independent of kinematic cuts in principle, but certain physics and apparatus-related corrections do depend on the experimental cuts. Hence, both methods lose some of their simplicity in real applications.

As in our earlier paper, our approach was to determine $\sin^2\theta_W$ directly by analyzing the $\sin^2\theta_W$ dependence of the ratio of accepted neutral-current events divided by

TABLE VII. The extracted charged-current valence-quark distribution referenced to $Q^2=10$ (GeV/c)^2 is tabulated as a function of x. The columns are defined with the same conventions as in Table V.

x bin	$xV_{\mathrm{CC}}(x)$	σ_{stat}	$\Delta[\sigma\theta_h(+)]$	$\Delta[\sigma\theta_h(-)]$	Δ_{scale}
0.015	0.0714	0.0691	−0.0966	0.1257	0.0155
0.045	0.2239	0.0885	−0.0869	0.1109	0.0442
0.080	0.4151	0.0729	0.0035	0.0093	0.0745
0.125	0.6326	0.0489	0.1324	−0.1206	0.0975
0.175	0.7936	0.0459	0.2057	−0.1959	0.0959
0.225	0.8643	0.0510	0.2157	−0.2034	0.0777
0.275	0.8714	0.0490	0.1726	−0.1607	0.0433
0.350	0.7743	0.0318	0.0643	−0.0456	−0.0085
0.450	0.5613	0.0153	−0.0897	0.0900	−0.0620
0.550	0.3385	0.0259	−0.1730	0.1524	−0.0820
0.700	0.1060	0.0204	−0.1230	0.1021	−0.0490
0.900	0.0039	0.0018	−0.0100	0.0081	−0.0039

TABLE VIII. The extracted charged-current sea quark distribution referenced to $Q^2=10\ (\text{GeV}/c)^2$ is tabulated as a function of x. The columns are defined with the same conventions as in Table V.

x bin	$xS_{\text{CC}}(x)$	σ_{stat}	$\Delta[\sigma\theta_h(+)]$	$\Delta[\sigma\theta_h(-)]$	Δ_{scale}
0.015	0.8441	0.1714	−0.3714	0.4559	−0.0470
0.045	0.8106	0.0930	−0.1709	0.1615	−0.0023
0.080	0.7034	0.0576	−0.0204	−0.0039	0.0190
0.125	0.5493	0.0477	0.0833	−0.0922	0.0270
0.175	0.3801	0.0387	0.0879	−0.0901	0.0190
0.225	0.2417	0.0263	0.0620	−0.0606	0.0100
0.275	0.1455	0.0161	0.0360	−0.0336	0.0029
0.350	0.0587	0.0060	0.0111	−0.0090	−0.0009
0.450	0.0142	0.0012	0.0007	−0.0003	−0.0012
0.550	0.0025	0.0002	−0.0004	0.0004	−0.0004

the number of accepted charged-current events for neutrinos, $R_\nu=\text{NC}^\nu/\text{CC}^\nu$, and the corresponding ratio $R_{\bar\nu}$ for incident antineutrinos. We have found that the extracted values of $\sin^2\theta_W$ and ρ were not very sensitive to the detailed Bjorken-x dependence of the underlying quark distribution functions so long as the x distributions were the same for both the neutral-current and charged-current interactions. Although it is not explicitly necessary to know the antineutrino to neutrino cross section ratio as required in the Llewellyn Smith method, we did need to know the antiquark content of the nucleon. For this determination we took the magnitude of the sea from the CCFRR[20] and CDHS[21] charged-current experiments.

The data for this determination are shown in Table II. The values of $\sin^2\theta_W$ and ρ were extracted by fitting the "experimental" ratios which contain the misclassified events. The misclassification was corrected by including the misclassified events in the theoretical Monte Carlo simulation rather than directly comparing the corrected ratios with theory. The former method has the advantage of correctly treating the subtle energy dependences of the misclassified events.

By fitting all four beam conditions described above (neutrinos and antineutrinos) for $\sin^2\theta_W$ with $\rho=1$, we found $\sin^2\theta_W=0.236\pm0.013$, where the quoted error was from the statistics of the measurement. The quality of the fit was $\chi^2=4.12$ for 3 degrees of freedom. The two-parameter fit where both $\sin^2\theta_W$ and ρ were determined yielded the result $\sin^2\theta_W=0.283\pm0.029$ and $\rho=1.043\pm0.024$. The two-parameter fit had a correlation coefficient of 0.883, and $\chi^2=1.78$ for 2 degrees of freedom. Fitting only the neutrino data yielded a value of $\sin^2\theta_W=0.238\pm0.013$, with $\chi^2=1.85$ for 2 degrees of freedom.

The principal source of the experimental systematic er-

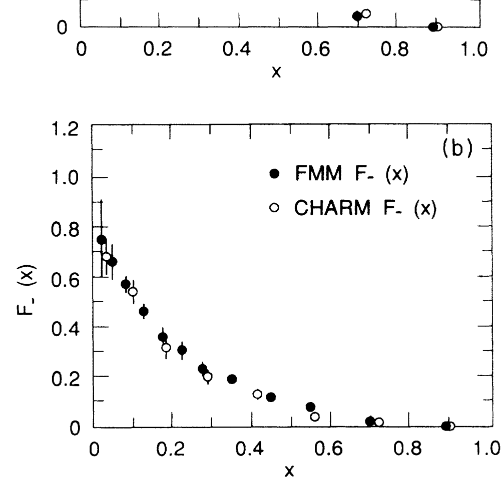

FIG. 15. (a) The comparison of the $F_+(x)$ distributions of this experiment (FMM) with those of the CHARM Collaboration (Ref. 35) for the neutral-current interaction. The errors displayed are from statistical sources only. (b) The comparison of the $F_-(x)$ distributions.

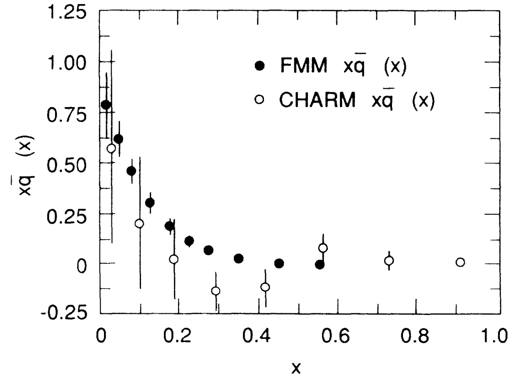

FIG. 16. The comparison of the sea-quark distributions, $x\bar q(x)$ of this experiment (FMM), and the CHARM Collaboration (Ref. 35). The error flags of the FMM data indicate the statistical uncertainty of the first four eigenvectors.

ror arose from the event misclassification, chief among which were the inaccuracies in modeling the effectiveness of the y cut in reducing the event misclassification, and the inaccuracies in modeling the efficiency of the μ-track finding program. The estimated value of the total experimental systematic error is $\delta \sin^2\theta_W = \pm 0.015$.

The major theoretical systematic error arose from the charm-quark mass used in the slow rescaling correction described above. We found from this source that $\delta \sin^2\theta_W = 0.015(m_c - 1.5)$, where m_c is the charm-quark mass parameter in GeV/c^2 used in the slow-rescaling correction. To estimate the resultant error we allowed the charm-quark mass to vary by ± 0.5 GeV/c^2 consistent with the statistical and systematic uncertainties in opposite-sign dimuon production in neutrino-nucleon scattering. This ambiguity in m_c results in an error $\delta \sin^2\theta_W = \pm 0.0075$. Other sources of error were estimated by allowing the strange sea content to vary within its measured limits, and permitting the nonstrange sea to change by ±10% over the Q^2 range of our data. All sources of theoretical systematic error added in quadrature was $\delta \sin^2\theta_W = \pm 0.01$.

V. CONCLUSIONS

We have tested the standard model by checking the prediction that the underlying quark distributions of the nucleon are independent of the gauge-boson probe. We found that the same quark distributions participate in deep-inelastic neutrino-nucleon scattering through the weak neutral current as through the charged current confirming this fundamental aspect of the model.

The determination of the quark structure of the nucleon by the weak neutral-current interaction was a difficult measurement since there were unavoidably large resolution smearing corrections. The x resolution was limited by the hadronic-shower-angle resolution, which was poor compared to that of the muon in charged-current events. The sensitivity of the deconvoluted x distributions to uncertainties in this resolution was the main systematic error of the measurement. The amplified statistical fluctuations in the deconvoluted x distributions were treated by truncating the eigenvector expansion at the point where the eigenvector contribution became statistically insignificant.

We have also determined from our neutral-to-charged-current ratio that $\sin^2\theta_W = 0.238 \pm 0.013 \pm 0.015 \pm 0.01$, where the first error is statistical, the second is from experimental systematic errors, and the third is from theoretical ambiguities.

ACKNOWLEDGMENTS

The authors would like to acknowledge the support of the National Science Foundation and U.S. Department of Energy. The generous technical assistance provided by the Fermilab staff, especially D. Burandt and R. Olsen, is gratefully acknowledged. D. Carpenter, R. Oudt, A. Raymond, and J. Thomson helped with the construction of the flash chambers and K. Krueger is thanked for his fine service of maintaining the detector. E. Druek was instrumental in constructing the proportional chambers and installing them in the calorimeter. S. Bristol, A. Cook, and C. Kerns were crucial in bringing the flash chamber readout system to a reality. D. Miller helped in the construction of the calorimeter sand and steel shot. N. Bosek did much of the mechanical engineering for the project. M. Warner helped with the structural steel. N. Michael tirelessly scanned events. D. Edmunds, R. Miksa, R. Richards, K. Danner, and T. Droege helped with the electronics of the flash-chamber HV system. D. Ritchie and G. Johnson helped with the on-line software. A. Malensek, G. Koizumi, and R. Stefanski are thanked for their indefatigable help in tuning the calibration beam. T. Kirk is thanked for his help in getting the experiment constructed and helping the effort through various growing pains. Special thanks go to M. Peters who participated in developing the off-line software and in the data taking, and to R. Fisk, T. Ohsugi, S. Mori, and J. Wolfson who helped in the early phases of this work.

---

[a] Present address: Stanford Linear Accelerator Center, Stanford, CA 94305.

[b] Present address: Fermi National Accelerator Laboratory, Batavia, IL 60510.

[c] Present address: Hughes Aircraft Co., Los Angeles, CA 90009.

[d] Permanent address: Argonne National Laboratory, Argonne, IL 60439.

[e] Present address: Union College, Schenectady, NY 12308.

[f] Present address: Bell Telephone Laboratory, Naperville, IL 60566.

[g] Present address: Institute of Physics, Warsaw University, Warsaw, Poland.

[h] Present address: Michigan State University, E. Lansing, MI 48824.

[i] Permanent address: Boston University, Boston, MA 02215.

[j] Permanent address: Illinois Institute of Technology, Chicago, IL 60616.

[k] Permanent address: University of Florida, Gainesville, FL 32601.

[l] Present address: University of Illinois at Chicago, Box 4348, Chicago, IL 60680.

[m] Permanent address: Centre d'Etudes Nucleaires de Saclay, B.P. No. 2, F-91191 Gif-sur-Yvette, France.

[1] This paper is derived largely from T. S. Mattison, Ph.D. thesis, Massachusetts Institute of Technology, 1986.

[2] The ratio test is reported by G. P. Yeh, Ph.D. thesis, Massachusetts Institute of Technology, 1984; S. Fuess *et al.*, in *Proceedings of the Eleventh International Conference on Neutrino Physics and Astrophysics*, Dortmund, West Germany, 1984, edited by K. Kleinknecht and E. A. Paschos (World Scientific, Singapore, 1985), p. 486; F. E. Taylor *et al.*, in *Proceedings of the Sante Fe Meeting,* Annual Meeting of the Division of Particles and Fields of the APS, Santa Fe, New Mexico, 1984, edited by T. Goldman and M. M. Nieto (World Scientific, Singapore, 1985); F. E. Taylor *et al.*, in *Proceedings*

of the Oregon Meeting, Annual Meeting of the Division of Particles and Fields of the APS, Eugene, Oregon, 1985, edited by R. C. Hwa (World Scientific, Singapore, 1985); D. Bogert *et al.*, Phys. Rev. Lett. **55**, 574 (1985). Preliminary data on the ratio test were presented by J. A. Slate, Ph.D. thesis, Michigan State University, 1985.

[3] S. L. Glashow, Nucl. Phys. **22**, 579 (1961); S. Weinberg, Phys. Rev. Lett. **19**, 1264 (1967); A. Salam, in *Elementary Particle Theory: Relativistic Groups and Analyticity (Nobel Symposium No. 8),* edited by N. Svartholm (Almqvist and Wiksell, Stockholm, 1968), p. 367.

[4] G. Altarelli and G. Parisi, Nucl. Phys. **B126**, 298 (1977).

[5] Recent measurements of $\sin^2\theta_W$ in deep-inelastic neutrino-nucleon scattering are CDHS Collaboration, H. Abramowicz *et al.*, Phys. Rev. Lett. **57**, 298 (1986); CCFRR Collaboration, P. G. Reutens *et al.*, Phys. Lett. **152B**, 404, (1985); CHARM Collaboration, J. V. Allaby *et al.*, Z. Phys. C **36**, 611 (1987); J. V. Allaby *et al.*, Phys. Lett. B **177**, 446 (1986); Fermilab-MIT-Michigan (FMM) Collaboration, D. Bogert *et al.*, Phys. Rev. Lett. **55**, 1969 (1985). A recent comprehensive review of the electroweak parameters is found in U. Amaldi *et al.*, Phys. Rev. D **36**, 1385 (1987).

[6] J. J. Aubert *et al.*, Nucl. Phys. **B272**, 158 (1986); F. J. Sciulli, in *Proceedings of the 1985 International Symposium on Lepton and Photon Interactions at High Energies,* Kyoto, Japan, 1985, edited by M. Konuma and K. Takahashi (RIFP, Kyoto University, Kyoto, 1986); F. E. Taylor, in *Neutrino 88,* proceedings of the 13th International Conference on Neutrino Physics and Astrophysics, Medford, Massachusetts, 1988, edited by J. Schneps, T. Kafka, W. A. Mann, and Pran Nath (World Scientific, Singapore, 1989); J. Feltesse, in *Proceedings of the XIVth International Symposium on Lepton and Photon Interactions,* Stanford, California, 1989, edited by M. Riordan (World Scientific, Singapore, 1990); S. Mishra and F. Sciulli, Annu. Rev. Nucl. Part. Sci. **39**, 259 (1989).

[7] A. Buras, Rev. Mod. Phys. **52**, 199 (1980); C. Quigg, *Gauge Theories of Strong, Weak, and Electromagnetic Interactions* (Benjamin/Cummings, Reading, Mass., 1983).

[8] M. Kobayashi and K. Maskawa, Prog. Theor. Phys. **49**, 652 (1973).

[9] G. Altarelli and G. Martinelli, Phys. Lett. **76B**, 89 (1978).

[10] L. W. Whitlow *et al.*, in *Proceedings of the International Europhysics Conference on High Energy Physics,* Madrid, Spain, 1989, edited by F. Barreiro and C. Lopez (North-Holland, Amsterdam, 1990), and references therein.

[11] C. G. Callan and D. J. Gross, Phys. Rev. Lett. **22**, 156 (1969).

[12] D. A. Edwards and F. J. Sciulli, Report No. Fermilab TM-660, 1976 (unpublished).

[13] T. E. Eldridge, Ph.D. thesis, Massachusetts Institute of Technology, 1986.

[14] D. Bogert *et al.*, IEEE Trans. Nucl. Sci. **NS-29**, 363 (1982); F. E. Taylor *et al.*, *ibid.* **NS-27**, 30 (1980); F. E. Taylor *et al.*, *ibid.* **NS-25**, 312 (1978).

[15] J. Bofill *et al.*, IEEE Trans. Nucl. Sci. **NS-29**, 400 (1982).

[16] S. Fuess *et al.*, in *Proceedings of the Gas Calorimetry Workshop,* Batavia, Illinois, 1982, edited by M. Atac (Fermilab, Batavia, 1982), p. 241; W. J. Womersley *et al.*, Nucl. Instrum. Methods **A267**, 49 (1988).

[17] M. A. Tartaglia, Ph.D. thesis, Massachusetts Institute of Technology, 1984.

[18] R. A. Magahiz, Ph.D. thesis, Massachusetts Institute of Technology, 1985.

[19] A. Mukherjee, Ph.D. thesis, Massachusetts Institute of Technology, 1986; A. Mukherjee *et al.*, Phys. Rev. Lett. **60**, 991 (1988).

[20] D. B. MacFarlane *et al.*, Z. Phys. C **26**, 1 (1984); M. V. Purohit, Ph.D. thesis, California Institute of Technology, 1984.

[21] H. Abramowicz *et al.*, Z. Phys. C **17**, 283 (1983).

[22] FMM-Florida (FMMF) Collaboration, B. Strongin, Ph.D. thesis, Massachusetts Institute of Technology, 1989.

[23] CDHS Collaboration, H. Abramowicz *et al.*, Z. Phys. C **15**, 19 (1982).

[24] CCFR Collaboration, K. Lang, Ph.D. thesis, University of Rochester, 1985; W. Smith, in *Neutrino 88* (Ref. 6); C. Foudas *et al.*, Phys. Rev. Lett. **64**, 1207 (1990).

[25] R. M. Barnett, Phys. Rev. D **14**, 70 (1976); J. Kaplan and F. Martin, Nucl. Phys. **B115**, 333 (1976); R. Brock, Phys. Rev. Lett. **44**, 1027 (1980).

[26] C. H. Llewellyn Smith and J. F. Wheater, Phys. Lett. **105B**, 486 (1981); J. F. Wheater and C. H. Llewellyn Smith, Nucl. Phys. **B208**, 27 (1982); **B226**, 547(E) (1983); A. De Rújula *et al.*, *ibid.* **B154**, 394 (1979).

[27] A. Sirlin and W. J. Marciano, Nucl. Phys. **B189**, 442 (1981).

[28] J. F. Gunion, Phys. Rev. D **10**, 242 (1974); R. Blankenbecler and S. J. Brodsky, *ibid.* **10**, 2973 (1974).

[29] D. Bogert *et al.*, Phys. Rev. Lett. **55**, 1969 (1985); the FMM result is also referenced in U. Amaldi *et al.*, Phys. Rev. D **36**, 1385 (1987).

[30] H. Harari, Phys. Rev. Lett. **24**, 286 (1970); J. Kuti and V. Weisskopf, Phys. Rev. D **4**, 3418 (1971).

[31] The effect of a violation of this relation from QCD effects is to reduce the small-x ($x<0.15$) and low-Q^2 values of the x distribution, dN/dx. Such a distortion is expected to be operative in both neutral-current and charged-current scattering and does not influence significantly the comparison of the two interactions.

[32] D. W. Duke and J. F. Owens, Phys. Rev. D **30**, 49 (1984). We used the "set 1" parameters. This reference includes a fit to the world's structure-function data, but cuts off the Q^2 evolution at $Q^2=4$ (GeV/c)^2. The same parametrization was used and compared with data. There was agreement beyond the intended kinematic range down to $Q^2=0.1$ (GeV/c)^2 (Ref. 1).

[33] R. Blair *et al.*, Phys. Rev. Lett. **51**, 343 (1983).

[34] Since we were primarily interested in a comparison of the neutral-current and charged-current nucleon structures we have simplified our analysis by neglecting the QCD correction factor $[1-\alpha_s(Q^2)/\pi]$, where α_s is the QCD coupling constant, which modifies the value of the GLS sum rule. For four quark flavors and $\Lambda=0.120$ GeV/c, in lowest-order QCD theory, the correction is about 7.3%.

[35] J. V. Allaby *et al.*, Phys. Lett. B **213**, 554 (1988).

[36] V. Blobel, in *1984 CERN School of Computing,* Aiguablava, Spain, 1984, edited by C. Verkerk (CERN, Geneva, 1985).

[37] E. A. Paschos and L. Wolfenstein, Phys. Rev. D **7**, 91 (1973).

[38] C. H. Llewellyn Smith, Nucl. Phys. **B228**, 205 (1983).